AFRICA CENTER OF EXCELLENCE FOR WATER MANAGEMENT

ADDIS ABABA UNIVERSITY

EVALUATING METHODS AND POLARIZATIONS OF S-1 SAR FOR TIME-SERIES FLOOD HAZARD MAPPING, AKAKI CATCHMENT

M.Sc. THESIS

TILAYE WORKU BEKELE

Advisor

Dr. Alemseged Tamiru Haile (IWMI)

June 2021

ACEWM/AAU, ETHIOPIA

EVALUATING METHODS AND POLARIZATIONS OF S-1 SAR FOR TIME-SERIES FLOOD HAZARD MAPPING, AKAKI CATCHMENT

BY

TILAYE WORKU BEKELE

A THESIS SUBMITTED TO THE DEPARTMENT OF HYDROLOGY AND WATER RESOURCES, SCHOOL OF POSTGRADUATE STUDIES, AFRICAN CENTER OF EXCELLENCE FOR WATER MANAGEMENT/ADDIS ABABA UNIVERSITY IN PARTIAL FULFILLMENT OF THE REQUIREMENTS FOR THE DEGREE OF MASTER OF SCIENCE IN WATER MANAGEMENT SPECIALIZATION OF HYDROLOGY AND WATER RESOURCES.

June 2021

ACEWM/AAU, ETHIOPIA

ADVISOR THESIS SUBMISSION APPROVAL SHEET

SCHOOL OF GRADUATE STUDIES

AFRICA CENTER OF ECELLENCY FOR WATER MANAGEMENT

ADDIS ABABA UNIVERSITY

This is to certify that the thesis entitled "**Evaluating methods and polarizations of S-1 SAR for time-series flood hazard mapping, Akaki catchment**'' submitted in partial fulfillment of the requirements for the degree of Master's with specialization in Hydrology and Water Resources, the Graduate Program of the Water management and has been carried out by Mr. Tilaye Worku Bekele under my supervision. Therefore, I confirm that the student has fulfilled the requirements and hence hereby can submit the thesis to the department for defense.

_____

Dr. Alemseged Tamiru Haile

(Advisor)

_____

Date

THESIS APPROVAL PAGE

This thesis entitled "**Evaluating methods and polarizations of S-1 SAR for time-series flood hazard mapping, Akaki catchment"** is approved by Advisor, Examiners, Chairperson and Head of Africa Center of Excellence for Water Management. It is fully adequate in scope and quality, as M.Sc research for the degree of Master of Science in Water Management, specialization in Hydrology and Water Resources.

Dr. Alemseged Tamiru Hail	_____	_____
Advisor	Signature	Date
Dr. Sirak Tekleab	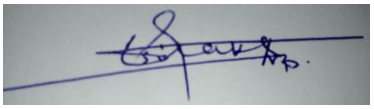	06-07-2021
External Examiner	Signature	Date
Dr. Getachew Tegegne	_____	_____
Internal Examiner:	Signature	Date
Dr. Beteley Tekola	_____	_____
Chairperson:	Signature	Date
Dr. Feleke Zewge	_____	_____
Head of ACEWM	Signature	Date

Declaration

I, Tilaye Worku Bekele, declared this thesis as it's my original work. This not has been presented in any university before and will not be present to any other university to award similar or any other degree.

_____

Signature

ACKNOWLEDGEMENT

Firstly and foremost, I would love to thank GOD for his mercy in the secureness of my life and health through this thesis work.

My special thank is forward to my advisor Dr. Alemseged Tamiru Haile, for his willingness to advise this thesis. He supplied relevant comments and suggestions when critically read my thesis. His, remarks and active response were vital to enrich my overall research discipline and scientific writing skills. Dr. Alemseged allowed me to participate in the short term trainings and scientific conferences to conduct this thesis work in advance. He shared the internet dongle in the pandemic time is the one great support to finish this thesis on time.

I would be advancing to thank communities situated in the flood-prone area for their incredible support when the field data is collected.

I like to thank the Ethiopia Geospatial Information Institute (EGII) for their support by implementing the necessary datasets to conduct this thesis.

It is my pleasure to acknowledge the Africa Center of Excellence for Water Management (ACEWM) and the Global Challenges Research Fund (GCRF) Water Security and Sustainable Development Hub for financially support this study. And the Arba Minch University (AMU) is my sponsor to follow this scholarship program.

Thanks to my family and classmates for their full encouragement.

ABSTRACT

Lack or absence of data is the main limiting factor for studying flood hazard and risk in many basins across the globe. The Google Earth Engine (GEE) has a potential to narrow data gaps by providing ease of access to remote sensing data and enabling automatic and rapid generation of flood inundation map for Near Real-Time monitoring. In this study, GEE was used to assess and analyze the Sentinel-1 (S-1) Synthetic Aperture Radar (SAR) dataset for flood inundation mapping in the Akaki catchment which hosts Addis Ababa city in the central part of Ethiopia. Ground Control Points were collected at the time of satellite overpass for evaluating the accuracy of the generated flood inundation maps. Change detection and Histogram thresholding methods were compared using co-polarized (VV) and cross-polarized (VH) images. A new method which is Root of Normalized Image Difference (RNID) was developed for change detection. Major flood affected roads in Addis Ababa city and Land Use Land Cover (LULC) classes were detected from April to November of 2017 to 2020. The result shows the RNID method performed better than the histogram thresholding for flood inundation mapping in the study area. The VH polarization performed better than the VV polarization to detect the lower signal backscatter intensity generated from the flooded surface. An overall accuracy of 95% and kappa coefficient 0.86 was obtained when applying the RNID method and VH polarization. In the Akaki catchment, the remote sensing mapping showed that the flood commonly starts in May and recedes in November, but flood was frequent and widespread from June to September. At the downstream of the new expressway, the riverine and pluvial flood frequently occurred in the past four years. The flood inundation map also showed that several major roads of Addis Ababa are affected by flooding. The irrigated and built-up area were the most affected land use classes with an inundation extent of 1057.05 ha (21.28% of the total irrigated land) and 544 ha (1.44% of the total urban area) respectively. The S-1 SAR was found useful for time series flood inundation mapping and the new change detection method (RNID) performed better in urban and peri-urban flood mapping, but the accuracy of the flood map varies with the flood detection method and the image polarization.

Key words: GEE, S-1 SAR, flood mapping, hazard, Addis Ababa, Akaki catchment.

TABLE OF CONTENET

List of Figure

List of Table

ABBREVIATIONS

API	Application Programming Interface
BOT	Bottom of Atmosphere
DEM	Digital Elevation Model
EGII	Ethiopia Geospatial Information Institute
EO	Earth Observation
ESA	European Space Agency
GCP	Ground Control Point
GEE	Google Earth Engine
GIS	Geographic Information System
GRDH	High Resolution Ground Range Detection
JRC	Joint Research Center
LULC	Land Use Land Cover
MCA	Multi-Criteria Approach
MSI	Multi Spectral Instrument
NRT	Near Real-Time
ROI	Region of Interest
RS	Remote Sensing
S-1	Sentinel-1
S-2	Sentinel-2
SAR	Synthetic Aperture Radar
RNID	Root of Normalized Image Difference
TBH	Tirunesh Beijing Hospital
TOA	Top of Atmosphere
TV	Temporal vegetation
VH	Vertical transmit Horizontal receive
VV	Vertical transmit Vertical receive

1 INTRODUCTION

1.1 Background

Flood inundation mapping is a pre-request for risk management. However, ground-based flood monitoring is difficult for the un-accessible study area (Bayik et al., 2018), a limited resource for in-situ measurement, low investments for flood hazard management, and a challenging environment. However, the remote sensing (RS) Earth Observation (EO) technology provides a large scale dataset without in-situ measurement to monitor the flood hazard at Near Real-Time (NRT) condition (Zeng et al., 2020).

The Sentinel-1 (S-1) Synthetic Aperture Radar (SAR) is advanced earth observation technology promising for flood hazard assessment (Zhuang et al., 2018). Providing a free S-1 SAR dataset to monitor the land surface is the one effort significance of the European Space Agency (ESA) Copernicus hub. The S-1 satellite collects the land surface information based on the intensity of signal backscatter reflected from the target area to the radar sensor (Devries et al., 2020). However, specular (small) signal backscatter intensity generated from the flooded surface marks dark on the radar sensor to simply differentiate the flood-affected pixels using different methods (Conde & De Mata Muñoz, 2019). Based on the direction of the signal transmitted and collected by the radar sensor, the S-1 free dataset is supplied as vertical-transmit vertical-receive, co-polarization (VV) and vertical-transmit horizontal-receive cross-polarization (VH) for land observation.

The polarization performance in flood detection is affected by the characteristics of the study area. The VV polarization contained a low incidence angle is recommended to detect the flooded pixel from the submerged area (Gumma et al., 2020). However, the VH polarization is sensitive to generate low signal backscatter intensity from the flooded surface are than the VV polarization (Kianfar, 2019) but, the combination of (VV and VH) polarizations are applied to reduce such discrepancy between the polarization during flood inundation mapping (Martinis & Plank, 2018). However, co-polarization and cross-polarization can lead to better performance in flood detection depending on the study area (Anusha & Bharathi, 2019)

Several methods have developed for rapid, automatic and accurate flood inundation mapping using the S-1 SAR dataset to Near Real-Time (NRT) monitoring. Based on user involvement to train the algorithm, these methods were categorized as automatic (Liang & Liu, 2020), semi-automatic and manual (Zhang et al., 2020). Nevertheless, all the methods use either multi-temporal S-1 dataset

(the dry and flooded image) (Conde & De Mata Muñoz, 2019) or single (target) image analysis (Schlaffer et al., 2015) for flood inundation mapping. However, all the methods are assumed low signal backscatter intensity is generated from the flooded surface.

Delivering a reasonably accepted flood inundation map is crucial for confidently manage the risk. The flood maps produced from the RS dataset is acceptable by the accuracies ranged statistically in the literature (Rwanga and Ndambuki, 2017; Nkomeje, 2017). However, some studies report the accuracy as qualitative (Long et al., 2014) and, some did not report the accuracy makes it difficult to decide the acceptancy of the flood maps (Ganji et al., 2019; Tavus et al., 2018). Primary dataset (Ground Control Points) and secondary dataset (another satellite image, modelled flood map) (Zeng et al., 2020) were used to validate the method and polarization of the S-1 dataset in flood inundation mapping. However, the statistical analysis that described agreement between the flooded and non-flooded surface was not well determined using a secondary dataset and GCPs collected at the non-overpass date of satellite.

Google Earth Engine (GEE) platform is powerful to rapidly process, analyze, and export flood hazard map by implementing JavaScript or Python code on Application Programming Interface (API). And, it makes simple for scientists, researchers, and developers to detect the land surface change (Mutanga & Kumar, 2019). GEE used in this study for accessing satellite images, processing and detecting the flood hazard. Therefore, the method applied on this study used to rapidly and automatically monitor the flood hazard for the urban and peri-urban area using the S-1 dataset.

1.2 Statement of problem

The problem of the flood hazard has increased in Akaki catchment hosted Addis Ababa city in the central part of Ethiopia (Birhanu et al., 2016). High flood hazard observed in Addis Ababa city during extreme rainfall due to the weak did drainage system and blockage (Addis Ababa City Road Authority) and peri-urban area affected by both riverine and pluvial flooding. The socio-economic, human life injury, health problem, traffic mobility were affected by this flood. The flood hazard damages the agriculture land, grazing land, environments (soil erosion), and water pumps (personal communication with flood-affected community in Akaki catchment). Most research has been done on flooding in Addis Ababa city and Akaki river by integrating different dataset and hydrodynamics models (Risi et al., 2020; Jalayer et al., 2014). These studies have determined the

probability of an area being at a flood risk. However, previously actual flood-affected area, roads and the spatiotemporal variability of the flood entire catchment were not determined and validated.

The long-term and sound recorded streamflow data is required to model the flood inundation map using the hydrodynamic model (e.g. the HEC-RAS) (Saad et al., 2019; Feyissa et al., 2018; SL et al., 2015). However, the hydrodynamic model is less active to rapidly and automatically generate the flood inundation map during a disaster due to requiring an in-situ dataset. Missing extreme flow data lead to reduce the model accuracy in flood inundation mapping along the river. Therefore, the lack of consistent streamflow data limits the applicability of the hydrodynamic models along the Akaki rivers.

The S-1 SAR has used for flood inundation mapping in Ethiopia (Martinis & Plank, 2018) and another part of the world (András Gulácsi and Ferenc Kovács, 2020; Devries et al., 2020). The parameter (polarization) of S-1 and the method used to detect flood affected area was selected depending on the previous literature (Tavus et al., 2018). But, suitable methods and polarization of S-1 are required for the study area to generate an accurate flood inundation map (Liang & Liu, 2020; Bioresita et al., 2018). Therefore, suitable method and S-1 parameter (polarization) are the pre-request for further (e.g. time-series) analysis.

Validating the method and polarization of S-1 in flood inundation mapping using ground-based data is rare. Dominantly, studies have used a secondary dataset (hydraulic model, optical satellite dataset) to validate the method and parameters of the S-1 dataset in flood mapping. However, this secondary dataset has collected after or before a day's S-1 satellite overpass (Dadhich et al., 2019; Zhang et al., 2020). Therefore, the agreement between the flooded and non-flooded surface at the NRT condition did not validate against secondary datasets.

1.3 Objective and research questions

The main objective of this study is to evaluate the S-1 SAR dataset corresponding to in-situ GCPs data for NRT flood hazard monitoring in the urban and peri-urban area of Akaki catchment.

The specific objectives of this study are listed as follow:-

- To compare multiple methods and polarizations of the S-1 SAR dataset for flood inundation mapping using in-situ GCPs.

- To evaluate the variability of flood frequency occurrence from April to November of 2017 to 2020 in the Akaki catchment.
- To determine flood hazard affected major roads in Addis Ababa city and LULC classes in the Akaki catchment.

The research questions of the study are read as: -

- Which method and polarization of the S-1 was perform better accuracies and suitable for flood inundation mapping in the Akaki catchment?
- Which is the high flooding season in the Akaki catchment?
- Which major roads in Addis Ababa city's and LULC classes were more affected by the flood hazard in the Akaki catchment?

1.4 Scope of the study

This study is limited to detect the time-series flood frequency occurrence maps using 80 S-1 SAR satellite image acquired from April to November of four years (2017 to 2020). The time series flood maps were categorized into five flood frequency occurrence classes (rare, sometimes, moderate, most and always) based on the percentage of repeatedly flood-affected pixels.

The GCPs collected from the flooded and non-flooded area at the date of the satellite overpass was used to validate the methods and polarizations of S-1 applied for flood inundation maps generated on 09 September 2020. The change detection and histogram thresholding methods applied separately using VV and VH polarizations of the S-1 SAR data in flood mapping. The dynamics of flood was determined by the percentage of flood inundated area corresponding to the Akaki catchment size. The interest of the domain area was selected at downstream stretched from the upstream of Tirunesh Beijing Hospital (TBH) near the dense forests until the Aba Samuel reservoir along the big Akaki River to show the spatiotemporal flood frequency occurrence map. This study reported level of flood inundated LULC classes and main roads in Addis Ababa city affected with flood in the past four years. The LULC map of the study was determined using the Sentinel-2 (S-2) optical satellite image that were acquired in different seasons of 2019. These, seasons are acquired from dry (non-rainfed) seasons and wet (rainfed) agriculture season. The accuracy of LULC map was determined corresponding to GCPs collected from the field.

1.5 Limitation of the study

This study is limited on applying and comparing the HH polarization of S-1 data in flood inundation mapping. The single threshold value for heterogeneous catchment was applied to detect the flood affected area. Fully spatially distributed GCPs were not used to validate the flood maps detected at the date of satellite overpass. Detail flood characteristics of depth and velocity were not evaluated. Lack of previous flood inundation maps on Akaki Rivers was limit to validate the time-series flood inundation maps generated in this study.

1.6 Significance of the study

It is impossible to avoid natural flood hazards. But, managing and adapting the flood hazard is crucial in the water resources and flood management to reduce the risk. However, understanding the extent of flood variability and affected area is the pre-request before implement flood management (action). Therefore, this study is significant as:

- It enhances the possibility for flood hazard monitoring using long time-series S-1 dataset for the area limit to apply the hydrodynamic models.
- This study used to indicate and determine major flood affected roads in Addis Ababa city for further improvement and maintenance of urban drainage and highly flood-affected sub-city.
- This study advantageous for land management to reduce the flood risks.

2 LITERATURE REVIEW

2.1 Overview of flood inundation mapping approaches

Many approaches are available for flood inundation mapping. Example of these approach include hydrodynamic models (Thakur & Sumangala, 2000), participatory based approach (Sullivan-wiley et al., 2019), Remote Sensing (RS) (Tsyganskaya et al., 2018). However, application of these methods is constrained by availability of hydrological data, investment for flood management, accessibility of the target area and area coverage (scale).

The Hydrologic Engineering Center's River Analysis System (HEC-RAS) hydrodynamic model has been widely used for flood inundation mapping (Fekadu et al., 2017; Saad et al., 2019). The model inputs are river geometry, upstream and downstream boundary condition, initial condition and manning's roughness coefficient determined from the land cover characteristics (Bucha & Selvaraj, 2019; Fekadu et al., 2017; Kari et al., 2014). However, input data are often missing or do not has the required accuracy for most flood plain. Hence, in-situ dataset requirement limit application of hydrodynamic model to rapidly generate flood inundation map during the disaster.

The participatory approach is a method that uses the communities' knowledge for flood hazard mapping (Singh, 2014). According to the author, it is suitable to apply for the area that hydrological data is scarce and resources to generate a flood hazard map. For instance, Sullivan-wiley et al., (2019) prepared the ground survey map, GPS track and digitized it on the desktop map. Questionaries' were employed for the community to allocate flood hazard area (depth, extent, and duration) (Klonner, 2020). The local community have high knowledge about the characteristics of flood to delineate (allocate) large flood affected area than non-local community (pedestrian). Overall, participatory approach require huge time, budget and human resources to generate time series flood map.

The RS Earth Observation (EO) technology integrated with GIS is another approach used to generate a flood inundation map at Near Real-Time (NRT) condition (Li et al., 2018). This approach is preferred for the non-accessible area (Bayik et al., 2018), hydrological data-scarce site and for project with low financial and human resources to delineate flood hazard area at large scale and repeatedly. It provide a long-term historical dataset to determine the flood extent variability (Broich et al., 2016). The detail for RS approach is present in the following subsections.

2.2 Overview of Remote Sensing (RS) for flood mapping

Advanced Earth Observation (EO) technologies are applied to monitor the flood at NRT condition (Zhang et al., 2020; Ganji et al., 2019). The RS satellites for land observation can be broadly categorized as (i) passive (optical) and (ii) active (radar) based on their electromagnetic radiation uses.

The optical RS satellites use solar radiation to operate the land surface from visible to infrared spectral bands, with high temporal resolution (e.g. daily for MODIS) than active sensor data (Zeng et al., 2020). However, the floods that occur at nighttime and in cloud contaminated weather condition limit their applicability for flood monitoring (Shen et al., 2019; Zhuang et al., 2018). Therefore, the optical satellite can provide useful data of the land surface only at daytime and in non-contaminated weather (cloud-free) condition. Landsat provide long term optical satellite dataset that is available freely to monitor the flood variability (Viana et al., 2019; Broich et al., 2016).

Advanced EO technology was demanded to overcome the limitation of optical satellite images for flood inundation mapping (Clement et al., 2017). The signal generated from the radar (active) RS satellite can penetrate cloud and hence operates in any weather conditions and time (day and night) (Martinis & Rieke, 2015; Zhuang et al., 2018). For instance, the ENVISAT Advanced SAR (ASAR) was launched in March 2002. It operates until the end of the mission in April 2012 (Schlaffer et al., 2015). The Sentinel-1 (S-1) Synthetic Aperture Radar (SAR) satellite was launched from Copernicus Open Access Hub of European Space Agency (ESA) in April 2014 (S-1A) and April 25, 2016 (S-1B) (Surampudi and Yarrakula, 2019; Li et al., 2018). The C-band SAR generate long-wavelength (7.5–3.8 cm) and low frequency (4–8 GHz) microwave electromagnetic radiation for land surface monitoring[1]. Additionally, there are more expensive and commercial ultra-high-resolution active RS satellites datasets that can be used for flood inundation mapping. These datasets are RADARSAT-2 (Nakmuenwai et al., 2017), TerraSAR-X, Constellation of Small Satellites for Mediterranean basin Observation (Cosmo-SkyMed) (Liu et al., 2019). Generally, the S-1 SAR image is the only active remote sensing dataset that are freely available is free available for users.

[1] https://earthdata.nasa.gov/learn/backgrounders/what-is-sar

2.3 Factor affecting the S-1 SAR image in flood mapping

Various factors affect the S-1 SAR dataset quality in flood detection. These factors are categorized as external factors (e.g. land surface heterogeneity, wind effect, terrain slope, temporal vegetation), internal factors (S-1 parameters) (e.g. polarization, incidence angle, and wavelength) and system of data acquisition (single platform) (Ganji et al., 2019; Kianfar, 2019). However, implementing different ancillary datasets can reduce the effects on the S-1 dataset capability for flood detection. These ancillary datasets are (e.g. permanent water body, and elevation dataset) (Zhang et al., 2020), sand layer (Martinis & Plank, 2018), land use land cover, Global Urban Footprint (GUF) dataset (Tsyganskaya et al., 2018).

From the urban area, heterogeneous signal backscatter intensities are generated causing the double bounce (DB), layover, and shadow effects on the radar sensor (Chini et al., 2019). Low signal backscatter intensity that is obtained from the flooded surface is sheltered by tall buildings that generate over brightness due to the effect of DB (Mahdianpari et al. 2019**).** And, high signal backscatter intensity generated from the land surface is blocked (shortening) by these, large buildings and the shadow appears dark imagining on the radar sensor (Gouveia et al., 2019). Generally, both high false-negative and false-positive flood alarms can be generated from urban area.

For instance, Chini et al., (2019); Yu Li et al., (2019), applied the Interferometric (InSAR) coherence based change detection. Tsyganskaya et al., (2018) implemented the Global Urban Footprint (GUF) dataset to mask the built-up area. According to Chini et al., (2019) the features that generate double bounce (DB) are extracted from series of dry season images. And, unusual low signal backscatter of the flooded pixel is detected. The phase difference observed between the two consecutive images was distinguished and, a threshold was applied to extract the flooded pixels (Yu Li et al., 2019). The local threshold value is implemented for each land characteristics of the heterogeneous area, rather than a global flood threshold (Anusha & Bharathi, 2019).

Steep terrain slope affects the signal backscatter intensity by generating over brightness tone and shadow on the radar sensor. For instance, when the sensor operation angle is less than the topography slope angle, the shadow will appear on the radar sensor to generate dark on the S-1 image (Zeng et al., 2020**;** Conde & De Mata Muñoz, 2019) and over brightness tone is generated when the signal returns from the hill area (Stephanie Long, 2014).

Hence, false-positive and false-negative flood will appear during flood inundation mapping using S-1 dataset. However, different studies have applied a threshold to mask the S-1 pixel that existed on the steep terrain slope area. For instance, Clement et al., (2017) applied 3^{o} slope to mask the pixels situated above the threshold value. However, Zeng et al., (2020**)** applied Head Above Near Drainage (HAND) and the threshold was determined based on the elevation difference observed between the drainage line and the land surface. The pixels situated above the threshold value are masked (Tsyganskaya et al., 2018; Yi Li et al, 2019). However, the HNAD method mask the pixel situated in high elevated area by following the drainage line rather than considering the widened area coverage.

Not fully submerged temporal vegetation (TV) can lead to generate over brightness tone during flood detection. Sandy area can confuse the radar sensor during flood detection by producing low signal backscatter intensity as the flooded surface (Schlaffer et al., 2015). The sandy area pore-space can transmit signals through to generate low signal backscatter intensity as the flooded surface (Martinis & Plank, 2018). However, such land surface is differentiated by analyzing the signal backscatter intensity of the dry season time-series image and then masked during the flood period to distinguish the low signal backscatter intensity generated due to the floods. However, the TV occurs during the flood period and, it generates high signal backscatter tone. The long-term time series analysis is used to differentiate such unusual high signal backscatter intensity generated by the TV's (Tsyganskaya et al., 2018). From all perspectives, analyzing time-series signal backscatter intensity is used to realize the characteristics of the study area (Tsyganskaya et al., 2018; Clement et al., 2017; Devries et al., 2020; Cian et al. 2018).

The S-1 parameters (polarization, wavelength, incidence angle) and the twelve days of revisits interval may influence in flood mapping (Tavus et al., 2018; Schlaffer et al., 2015). Unique characteristics that generating low signal backscatter intensity from the flooded surface perform differently depending on the factor of the incidence angle of the radar image (Manjusree et al., 2012). Therefore, selecting the appropriate S-1 polarization is with a major task with during flood detection. For instance, Kianfar, (2019) recommend the cross-polarization (HV or VH) of the S-1 for flood detection. This polarization is characterized by high-incident angle and low ripple backscatter intensity performance from the flooded surface than the co-polarization (VV). The VV polarization was recommended to detect the flooded pixel from the submerged area (Bayik et al.,

2018; Gumma et al., 2020). According to Martinis & Plank, (2018) dual-polarization (VH and VV) is used to minimize; such discrepancy in selecting the type of polarization in flood detection.

Between the sequences of twelve days revisit interval of the S-1 SAR satellite, some flood information is missed. However, to reduce such limitation of the S-1 in flood monitoring, it is integrated (fusing) with another optical satellite dataset since, S-1 is the only radar image that is freely available (Zeng et al., 2020; Anusha & Bharathi, 2019). In table 2.1 common external and internal factors that affect the accuracy of the S-1 SAR dataset for flood inundation mapping are summarized and techniques applied in reducing such factors are shown.

Table 2.1 Some of the external and internal factors that affect the Sentinel-1 (S-1) SAR dataset and applied techniques to reduce the effects

Reference	**Error source**		**Effect**		**Applied solution for**	
	External	Internal	Satellite image	Flooded pixels	External factor	Internal factor
Anusha & Bharathi, (2019); Tsyganskaya et al., (2018)	Heterogeneous land surface	S-1 Parameters	DB, layover, shadow, speckle noise,	Increasing (false positive) and Reduce (false negative)	Interferometric Coherence based change detection, Masking the built-up area using (GUF), local threshold was applied	Dual polarization was implemented, viewing angle correction
Zeng et al., (2020), (Stephanie Long, 2014)	Topography	Revisit time	Shadow and over brightness	Increase false flood alarm and hide the flooded area	Terrain slope and elevation (HAND) based masking	Integrate (fuse) different satellite dataset
Martinis & Plank, (2018),	Permanent sand surface		Generate low signal backscatter intensity.	Increase false flood alarm	Time series analysis and applied sand exclusion layer	
Tsyganskaya et al., (2018),	Temporal vegetation		Over brightness tone	Hide the flooded pixel	Normalizing the time-series signal backscatter intensity to differentiate un usual intensity	

2.3.1 S-1 SAR image pre-processing

The S-1 image pre-processing is challenging relative to the optical dataset (András Gulácsi and Ferenc Kovács, 2020; Devries et al., 2020). However, pre-processing image is the pre-request before detecting the flood affected pixels.

Precise orbit files (accurate satellite position information) (Tavus et al., 2018; Ganji et al., 2019), border noise removal (invalid data from scene edge), thermal noise removal (noise in sub-swath), radiometric calibration (provide unit less signal backscatter), terrain corrections (co-register with the DEM) (Devries et al., 2020) and speckle filtering (to reduce the granular like noise) are the common required pre-processing activities during flood inundation mapping.

Speckle is a noise like granular-pattern that occurs in SAR image due to contrasting variation of signal backscatter when collected in a single platform and the signal wave interface with small particle (Devries et al., 2020; Bayik et al., 2018). Different methods have been implemented to reduce the speckle noise via protecting important information (features) in various window size based on the characteristics of the target area and objectives of the study. These methods are Gamma-Map (Ganji et al., 2019), Lee (Zeng et al., 2020), Refined Lee, mean, median (Kianfar, 2019; Anusha & Bharathi, 2019), Boxcar (Zhang et al., 2020), Frost, Lee sigma (Conde & De Mata Muñoz, 2019). The median filter is applied for the area characterized with high signal backscatter variability. According, to Conde & De Mata Muñoz, (2019) the Gamma Map filter is developed based on the Bayes statistical analysis that is suitable to apply for extensive area of the field (forest, ocean). The Lee filter use the statistical parameters of the mean and standard deviation of the signal backscatter intensity to level heterogeneity generated from the deep area (due to the steep slope topography). Different window sizes (pixel by pixels) (3x3, 5x5, 7x7, and 11x11) are implemented to smoothing the rough backscatter intensity. For instance, Yommy et al., (2015) applied a small (3x3) window size, whereas (7x7) window size was visually selected by (Tavus et al., 2018). Overall, a high false-positive flooded pixel is generated randomly from an unfiltered satellite image (Conde & De Mata Muñoz, 2019). However, large window size leads to blurred satellite image and lost important features information (Gumma et al., 2020; András Gulácsi and Ferenc Kovács, 2020).

2.3.2 Google Earth Engine (GEE)

GEE is a cloud-based computing platform that combines a multi-petabyte catalogue of satellite imagery and geospatial dataset with planetary scale. JavaScript and Python can be applied on the Application Programming Interface (API) to rapidly process, analyze, detect and export the land surface changes. Such makes it simple for scientist, researchers, and developers[2]. GEE is implemented for different applications in land and water resource management. For instance, Devries et al., (2020); Wang et al., (2018); Xia, et al., (2017) generate flood inundation map and surface water dynamics, Venkatappa et al., (2020); Dacosta et al., (2019) detected forest land cover change. Generally, GEE does not require large computer storage and high processor unit, to analyze, detect and export long term earth surface change using multiple satellite and geospatial datasets (Devries et al., 2020; Skakun et al., 2014).

2.4 Methods used for flood inundation mapping

Numerous methods have been developed to generate accurate, rapid and automatic flood inundation maps using the S-1 SAR dataset (Nakmuenwai et al., 2017). However, based on the user involvement for flood detection, these methods are categorized into fully automatic (Li et al., 2018; Chini et al., 2019; Liang & Liu, 2020), semi-automatic and manual (Zhang et al., 2020). The semi-automatic is requires another additional flood classification process like machine learning and training dataset (Zhang et al., 2020) (e.g. random forest classification). According to the author, such a semi-automatic method is rare to detect the flood pixel without actual observation. However, the automatic methods do not require user involvement (field dataset) to train the algorithm for flood detection. For instance, Yu Li, et al., (2019); Li et al., (2018) were classified the image by using automatic detection and, the threshold was applied to cluster flooded pixel. As a result the authors can apply the method for a long time-series flood inundation mapping (e.g. change detection). However, all the methods are categorized into multi-temporal image analysis (e.g. change detection, Red Green Blue (RGB) composition) (Conde & De Mata Muñoz, 2019) and single image analysis (e.g. histogram thresholding, fuzzy logic, regional growing, texture analysis) (Schlaffer et al., 2015). However, low signal backscatter intensity is obtained from the flooded surface (Martinis & Plank, 2018).

[2] https://earthengine.google.com/

Histogram thresholding is a method that analyzes a single (target) image to detect the flooded pixels. It is widely used due to the simplicity, flexibility and effectiveness (Gumma et al., 2020) of the method in flood mapping. The method was developed based on the histogram of signal backscatter intensity generated from the flooded and non-flooded surface (Kianfar, 2019; Bayik et al., 2018; Tavus et al.,2018) and the threshold value applied to differentiate the flooded and non-flooded surface (Conde & De Mata Muñoz, 2019). The pixel that contained less signal backscatter intensity than the threshold value is categorized as a flooded pixel (Lin et al., 2019).

However, the pixel area coverage of the flooded and non-flooded area influences the simplicity of the method. For instance, Liang & Liu, (2020) divided the study area into a proportional area of the water and the land surface. But, according to Tavus et al., (2018); Kianfar, (2019) the average flood threshold values are determined from selected region of interest (ROI) area (reservoir, lake, river, water tank). However, the signal backscatter intensity obtained from the permanent (large) water surface and, the temporal flooded area has slight differences due to depth, feature situated, temporal vegetation in the flooded surfaces (Manjusree et al., 2012). Therefore, an ancillary dataset (e.g. sand exclusion layer) (Martinis & Plank, 2018), field inventory (training dataset), and other algorithms (Zhang et al., 2020) are required to determine the optimal flood threshold in histogram thresholding method.

Change detection is a method that analyze multi-temporal satellite images to obtain the layers difference of the dry season (reference) and flooded (target) image (Tavus et al., 2018). Different change detection methods were described in the review papers (Lu & Moran, 2004; Hussain et al., 2013). From these methods the image difference (Clement et al, 2017; Long et al., 2014), image rationing, log-ration (Bayik et al., 2018; Li et al., 2018) are applied widely to detect the change from multiple satellite-images. These methods are quick and simple to apply in the change detection method (Stephanie Long et al, 2014). But, additional clustering algorithm is implemented to differentiate the interest (flooded) pixels (Clement et al., 2017). These change detection methods reduce the factors affecting the S-1 dataset in flood detection due to the change layer used between the reference and flooded image (Li et al., 2018). However, the reference image affects the change detection method performance in flood mapping (Schlaffer et al., 2015; Hostache et al., 2012).

For instance, Tavus et al., (2018); Reksten & Solberg, (2019) randomly selected the reference image that acquired before the flood events. However, collecting the reference image from fully

driest season is suitable to reduce the soil moisture effect and leads to obtain maximum difference between the dry (reference) and flooded season image (Li et al., 2018). The same parameters of the S-1 (polarization, sensor mode, orbit track, area of coverage, wavelength and incidence angle) are applied for the reference and target (flooded) image to reduce the parameter effect in flood mapping (Clement et al., 2017). However, collecting from the same year is optional (Hostache et al., 2012).

2.5 Validation

The flood maps generated from the RS dataset required validation before any further use. However, the maps acceptability is dependent based on the acceptable accuracy levels determined in the literatures (Rwanga and Ndambuki, 2017; Nkomeje, 2017). The error matrix is a widely applied for accuracy assessment in quantitative form (Bayik et al., 2018). However, some studies also described the accuracy in qualitatively form (Long et al., 2014) and some did not determine the accuracy yet (Ganji et al., 2019). However, the ways of accuracy description is dependent with the dataset used for validation. For instance (Schlaffer et al., 2015; Stephanie Long, 2014; Dadhich et al., 2019, Martinis & Plank, 2018, Kianfar, 2019; Long et al., 2014) applied secondary datasets to validate the S-1 dataset for flood inundation mapping. These secondary datasets are optical satellite image, previous hydraulic models, previous studies (flood management operational maps) (Zhang et al., 2020; Devries et al., 2020), local community information, land cover map (Dadhich et al., 2019), GeoEye-1 high-resolution airborne imagery (Zeng et al., 2020). However, these dataset can introduce additional error that were not caused by the S-1 dataset at Near Real-Time condition (Bayik et al., 2018; Chini et al., 2018).

2.6 Flood hazard assessment

Flood hazard is described from different perspectives. For instance, the effects of flood hazard on the land (soil) degradation is from environmental perspectives, whereas the flood hazard effect on the human activity is from socio-economic perspectives. Flood is a natural phenomenon but become a hazard (potential source of harm) when people of socio-economic interest in the affected area such as agricultural land, socio-economic activity, environmental assets in a specific area and period (Argaz et al., 2019; Rose et al., 2014). However, the magnitude of the flood hazard is described from perspectives of flood characteristics (depth, velocity, duration) and vulnerable assets (population, structure, economic assets) (Duan & Liu, 2014).

Remote Sensing (Rose et al., 2014) and hydrodynamic models integrated with GIS (Tingsanchali et al., 2010) are the techniques widely used for flood hazard assessment. The hydrodynamic models determine the flood hazard characteristics along the river (Thapa et al., 2020). For instance, Tingsanchali et al., (2010) classified the flood hazard zone using critical depth which is recommended by the flood-plain development manual. Arseni et al., (2020) was categorized the flood hazard zone based on depth of flood obtained in the different return period.

The RS technology can be used for flood hazards assessment at any scale. For instance, Gashaw & Legesse, (2011); Rose et al., (2014) determined the flood hazard area corresponding to flood extent inundated on different LULC classes. To determine the flood hazard sensitive area Multi-Criteria Approach (MCA) is applied based on the factors that alter the characteristics of the flood (soil, elevation, terrain slope, land cover, drainage density and spatially distributed rainfall intensity) (Argaz et al., 2019; Gashaw & Legesse, 2011). For instance, Argaz et al., (2019), Wondim, (2016) classified areas that sensitive to flood hazard as very low, low, moderate, high and very high. As the author the flood hazard has expanded in a different part of Ethiopia.

In Ethiopia, twelve river basin are available. From these, the Awash river basin (lower, middle and upper-Awash sub-basin), Baro-Akobo basin (Woube, 1999), Wabi Shebelle basin are listed as flood-affected basins in Ethiopia (Wondim, 2016). The local floods were observed on the Lake Awassa, Lake Besseka, Dire Dawa towen, Ribb and Gumara area of (Fogera Plain)**.** In Oromia, Gambella, SNNP and Amhara regions highly flood affected area are observed[3]. For instance, Gumma et al., (2020) generated time series flood inundation maps in the Afar region using the S-1 SAR dataset. In the Awash River the flood hazard zone is determined using MCA using GIS and, HEC-RAS hydrodynamic model to generate flood hazard zone along the river (YS et al., 2015; Fekadu et al., 2017). Generally, in Ethiopia, the flood hazard occurs due to overtopping of the water from the river bank (during extreme rainfall), poor drainage system, overflowing of reservoir excess water (Woube, 1999).

2.7 Limitation of previous flood inundation mapping studies

Various limitations are perceived in flood inundation mapping using the S-1 SAR dataset. From these selecting suitable method and polarization for the study area (Bayik et al., 2018), the

[3] https://floodobservatory.colorado.edu/Events/4965/2020Ethiopia4965.html

secondary dataset used for validation, way of accuracy description (qualitative, and not determined) are common problems in flood mapping by using the S-1 dataset. For instance, Liang & Liu, (2020); Bioresita et al., (2018) determine the study area characteristics effect in flood mapping using S-1 dataset. However, various studies selected their method and polarization of S-1 based on the previous literature recommendations (Tavus et al., 2018). Numerous studies did not evaluate the S-1 dataset in flood detection at NRT condition.

For instance, Kianfar, (2019) used S-2 optical satellite image that acquired two days before S-1A and four days after S-1B. Martinis & Plank, (2018) collected the optical satellite image five days later than the of the S-1 overpass.

3 MATERIAL AND METHODS

3.1 Description of the study area

The Akaki catchment is a sub-basin of the Awash River Basin and it host the Addis Ababa city at the central part of Ethiopia. Three water supply reservoirs (Dire, Legedadi, and Gefersa) are found at the upstream and the Aba Samuel reservoir (hydropower plant) is exist at the outlet of the catchment (Figure 3.1). The catchment is defined geographically by 453336.92 to 507726.06 E and 1019606.4 to 970155.43 N that covers 1459.33 square kilometer.

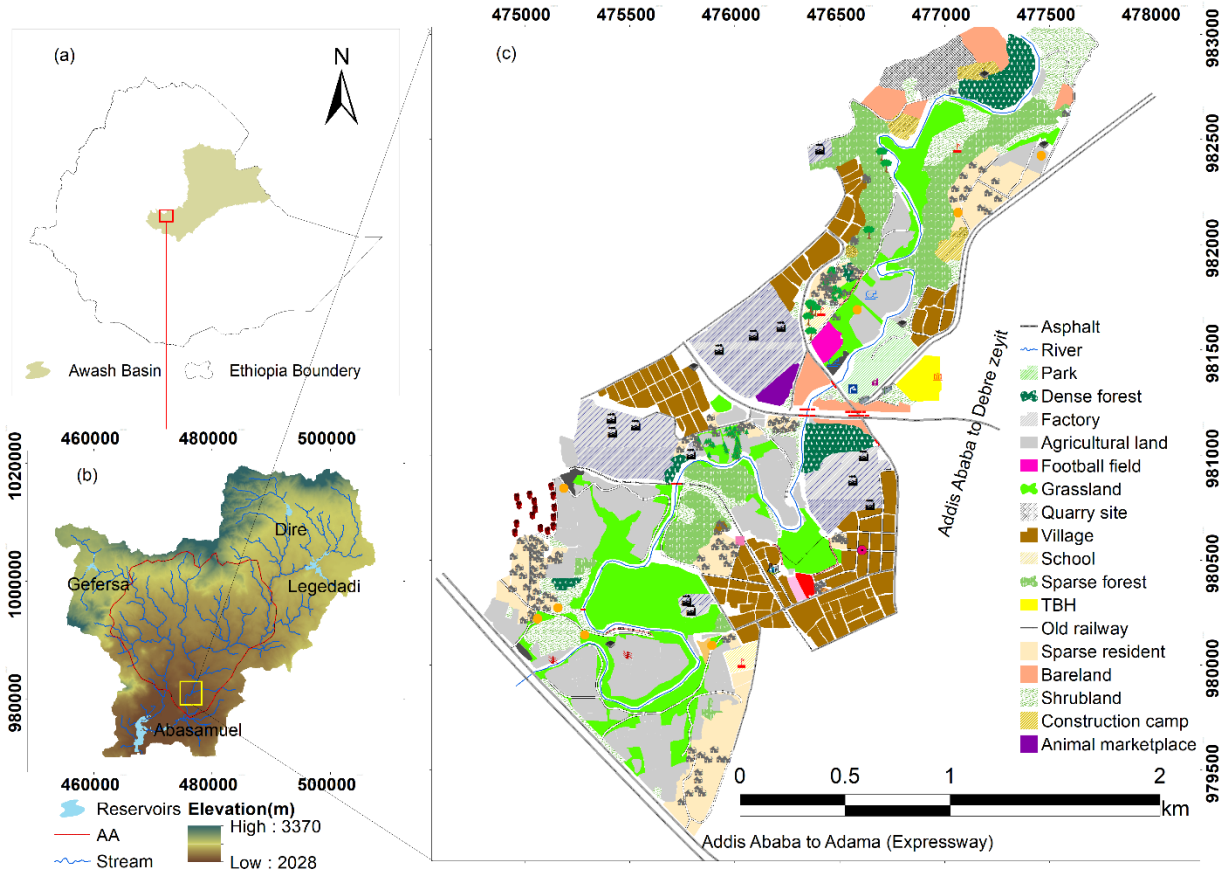

Figure 3.1 Location and characteristics of the study area

Two main big rivers (big Akaki and little Akaki) drain the Akaki catchment to feed the Aba Samuel reservoir. However, the Bulbula and Kebena river join to form the big Akaki river. See the confluence of these streams on Figure 3.2. The Kebena river drains the north part of the catchment (old part of the Addis Ababa city). Several small tributaries Bantykentu, Kurtme, Kostre, and Kechene are the tributaries of the Kebena river. Bulbula river drain north-east part of Akaki and is

feed by the Legedadi river on its most upstream part which is surrounded by small towns of (Dire, Legedadi and Sendefa). The flood release by the reservoirs (Legedadi and Dire) is received and conveyed by this river.

The little Akaki river is the main river draining the North West (NW) part of the catchment to feed the Aba Samuel reservoir. It conveys water released from the Gefersa reservoir toward the flood plain and then the Aba Samuel reservoir. Generally, the Akaki catchment drainage system has three sub-systems. These are (i) the water drained from northern and central part of the catchment is collected by the Kebena river, (ii) the water drain from NE part of the catchment to feed Aba Samuel reservoir is collected by Legedadi river which drain to feed the Bulbula river and, (iii) the water drained from NW part of the catchment to feed the Aba Samuel reservoir is collected by the little Akaki river.

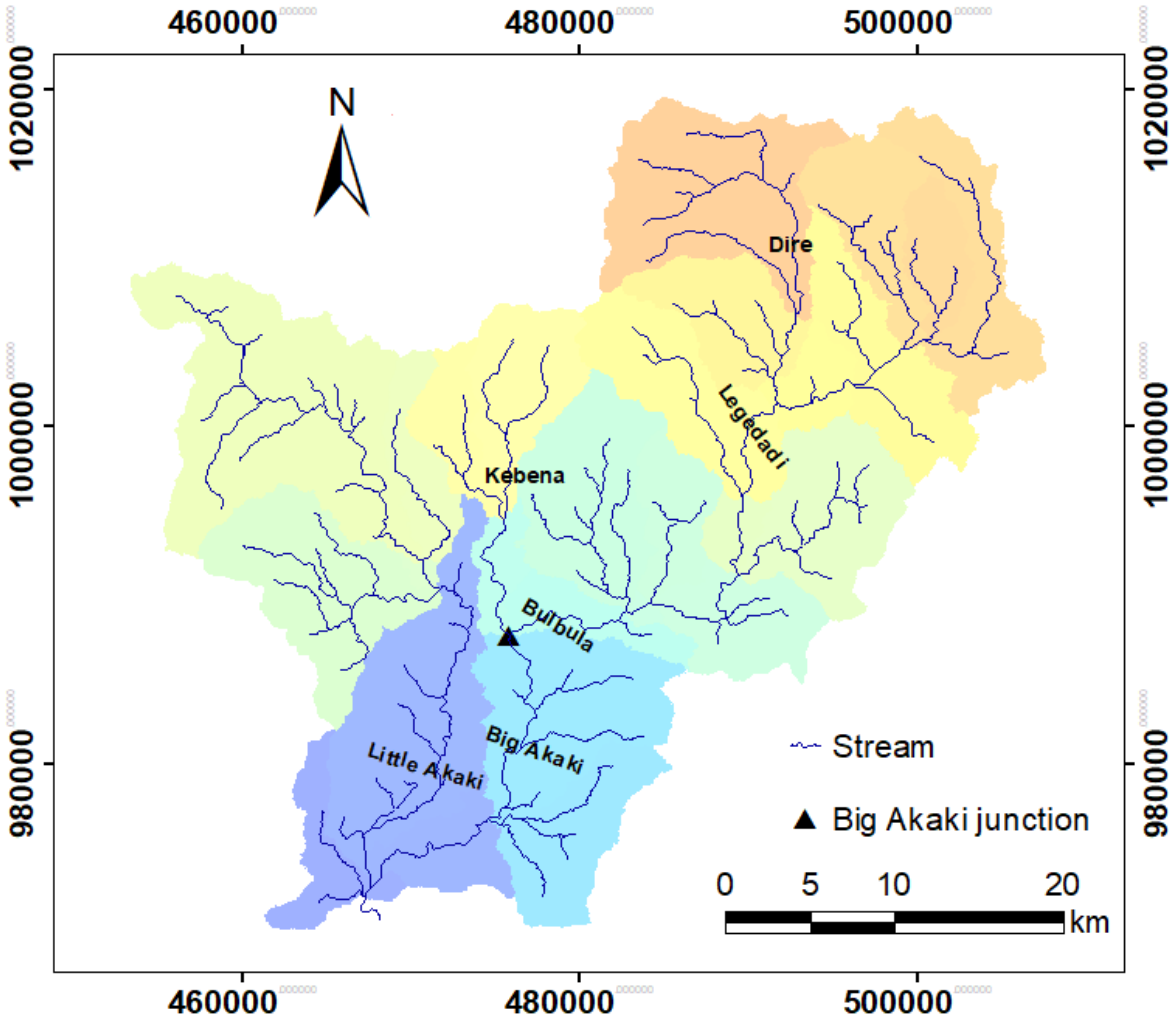

Figure 3.2 Drainage system of the study area

3.2 Elevation and terrain slope.

Elevation of the Akaki catchment varied from 2028 m a.m.s.l to 3370 m a.m.s.l. The maximum elevation is found at the upstream boundary (north) part of the catchment (Entoto Mountain) and the minimum elevation is found at the downstream low-laying part of the catchment (Figure 3.2 (a)).

The terrain slopes are classified into seven different groups based on the FAO standards. The slope class situated from 0-2% is flat, 2-5% is gentle, 5-8% is slopping, 8-15% is strongly slopping, 15-30% is steep, 30-60% is very steep and >60% is extremely steep. The extreme steep slope is found at the north upstream (boundary) of the catchment, SW part of the catchment, and followed some drainage line of the stream. At the downstream and NE part of the catchment flat slope is perceived (Figure 3.3 (b)). Based on the above slope classes 7.7%, 25.9%, 19.9%, 25%, 14.5%, 6.7% and 0.3% of the catchment area is laid in flat, gentle, slopping, strong sloping, steep, very steep, extreme steep slopes respectively.

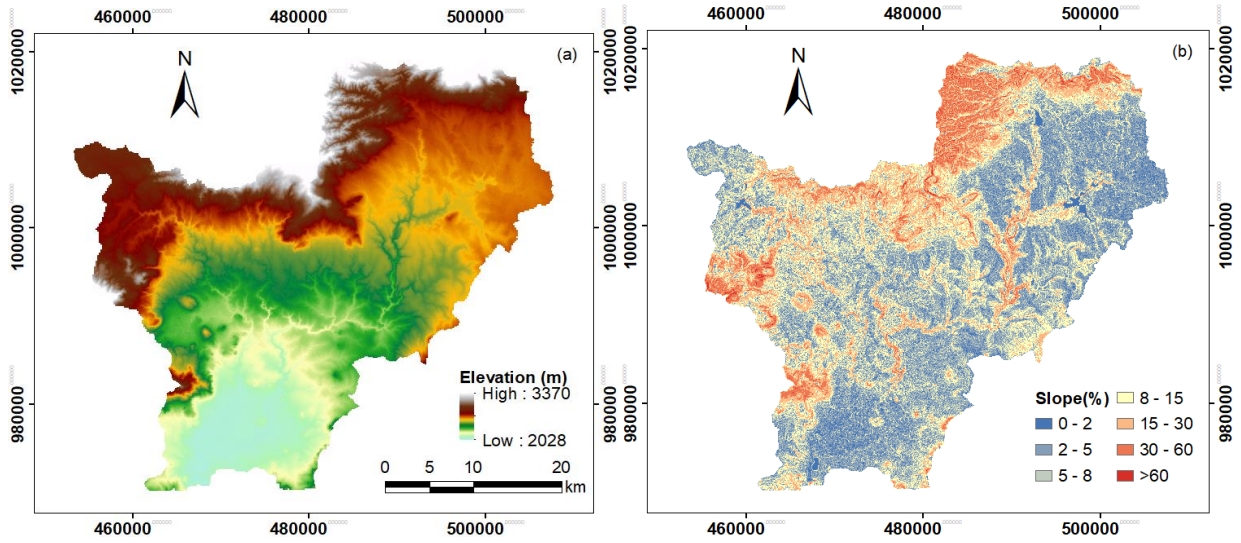

Figure 3.3 Elevation (a) and slope (b) map of the study area

3.3 Land Use Land Cover (LULC)

In this study, seven LULC classes of the Akaki catchment are observed. These LULC classes are built-up area, rainfed-agricultural land, irrigated (non-rainfed) agricultural land, bare-land, grassland, mixed forest and, water body. The large part of the catchment was covered by the rainfed agricultural land and built-up area. The asphalt roads, resident, commercial, industrial,

paved covered land were laid in the built-up area and affect the hydrological responses (runoff generation). The irrigated agriculture land is dominated at the downstream followed with both the little and big Akaki river. The detail land use land cover classes is described in section 5 of this document.

3.4 Materials

For this study, multiple datasets and software were used for flood inundation mapping and flood hazard assessment. Multi-temporal Sentinel-1 (S-1) Synthetic Aperture Radar (SAR), Sentinel-2 (S-2) optical satellite image, google earth image, Ground Control Points (GCPs), Digital Elevation Model (DEM), global dataset (Global Surface Water (GSW) and national dataset (administrative boundaries of Addis Ababa's sub-city) were used. The Google Earth Engine (GEE) is implemented to collect satellite images and global dataset. The national dataset is collected from the Ethiopia Geospatial Information Institute (EGII) and the GCPs is collected from the field to the study area.

GEE is a cloud computing platform implemented to access, process, detect, extract and export the time-series flood inundation maps and Land Use Land Cover (LULC) map of the study[4]. However, additional software (Geographic Information System (GIS), Microsoft Excel and Google Earth) were applied to analyze the flood inundation maps and the LULC map generated from GEE. The Global Positioning System (GPS) was used to track, register and collect the (x, y) coordinate of GCPs from the flooded surface, non-flooded surface, key-features situated in the flood-prone area and from different land cover surface.

Table 3.1 Overview for dataset and software implemented in this study

Dataset				**Software**
Satellite dataset	Global dataset	National dataset	Field dataset	
				GEE
S-1 SAR	GSW	10m DEM	GCPs	GIS
S-2 optical		Shapefile of Addis Ababa		Excel
Google earth image				Google Earth

[4] https://developers.google.com/earth-engine/datasets/catalog

3.4.1 S-1 SAR

The C-band Sentinel-1 (S-1) SAR satellite was launched by the European Space Agency (ESA) Copernicus Hub. The first sentinel-1 (S-1A) was launched on April 3, 2014 whereas the second satellite (S-1B) was launched on April 25, 2016. Hence, both satellites has the same parameters (signal frequency, long wavelength radiation, incidence angle, polarizations, and orbit pass) and positioned at 180^{o} phase difference. The couple of S-1 A and S-1 B is operates with 6-days interval over Europe (Li et al., 2018), but 12 days interval for the rest of the earth surface (Devries et al., 2020).

The S-1 SAR image is delivered in four different modes based on the area of interest and swath width. These four imagery modes are Interferometric Wide Swath (IW), Stripmap (SM), Extra-Wide Swath (EW) and Wave (WV). From these IW imagery mode that contained vertical transmit-vertical receive co-polarization (VV) and vertical transmit horizontal receive cross polarization (VH) is launched for land observation and flood monitoring (Conde and De Mata Muñoz, 2019, Clement, et.al 2017). Originally, IW is delivered as 5x20m (range x azimuth) resolution by the Single Lock Complex (SLC) image format. However, in the level-1 process the IW image was resampled to 10x10m (pixel spacing) as High resolution Ground Range Detection (L-1, GRDH) format that loaded on the GEE[5].

3.4.2 S-2 MSI

In this study, the Sentinel-2 (S-2) Multi Spectral Instrument (MSI) optical satellite image that was launched from European Space Agency (ESA) used for LULC classification. It consist of two consultation missions of S-2A launched on (23 June 2015) and S-2B launched on (7 March 2017) are positioned at 180^{o} phase difference on the same orbit. Pre-processed S-2 level-2A dataset that has 12 spectral-bands and consisted of 10-60m spatial resolutions was implemented for this study (table 3.2). The S-2 satellite revisit on ten day interval at the equator with one satellite and 5 days for the rest at the cloud free condition (Huong Thi et al.,2020). In Akaki catchment the S-2 dataset is provided every 5 days interval.

[5] https://sentinel.esa.int/web/sentinel/user-guides/sentinel-1-sar/acquisition-modes/interferometric-wide-swath

3.4.3 Global dataset

The Global Surface Water (GSW) dataset was developed by Joint Research Center (JRC) of European Commission using all Landsat's image available in GEE[6]. It was developed from 3,865,618 scenes of the Landsat 5, 7, 8 image of 30 m resolution from 16 March 1984 to 31 present. The images were classified into water and non-water body using change detection approaches applied between the time periods of (1984-1999, 2000-2018) (Pekel et al., 2016). In this study, the GSW dataset used to mask the permanent water bodies to differentiate from actual floods.

Table 3.2 Characteristics of the S-2 Multi Spectral Instrument (MSI)

Band name	Resolution	Wavelength	Description
B1	60	443	Aerosol
B2	10	490	Blue
B3	10	560	Green
B4	10	665	Red
B5	20	705	Red Edge 1
B6	20	740	Red Edge 2
B7	20	783	Red Edge 3
B8	10	842	Near Infrared(NIR)
B8a	20	865	Red Eadge 4
B9	60	940	Water vapor
B11	20	1610	Short wave Infrared (SWIR 1)
B12	20	2190	SWIR 2

3.4.4 National dataset

The 10m spatial resolution DEM and shapefile of administrative boundaries of Addis Ababa's sub-city are collected from the Ethiopian Geospatial Information Institute (EGII). The DEM was generated by aerial photogrammetry in 2018. This DEM served as input data to drive these terrain slope that was used as a parameter for flood inundation mapping. The administrative boundaries of the Addis Ababa's sub-city was delineated by EGII in 2019.

[6] https://developers.google.com/earthengine/datasets/catalog/Joint Research Center(JRC) GSW1_1_GlobalSurfaceWater

3.4.5 Field data

In this study, the field visit has been undertaken in three different seasons of (i) before the 2020 flood period that stretched from October, 2019 to December, 2019, (ii) during flood period that stretched from July, 2020 to October, 2020 and (iii) after the flood period in December, 2020.

Firsts, the flood-prone area situated at the downstream was frequently visited before the flood period of 2020 (October, 2019 to December, 2019). In this time period, several activities were undertaken by following a systematic approach to determine the boundaries for the interest of domain area. During this period the researcher (i) explore the flood-prone area from google earth image (ii) interviewed community situated in the flood-prone area about the historical flood characteristics, visited the flood mark of tree and flood damaged assets, (iii) registered and tracked the (x, y) coordinates of the key features existed in the flood plain (roads, railways, factories compound and large villages block etc.) by using GPS, (iii) allocated boundaries for the interest of domain area that used to show spatial flood frequency occurrence maps in Akaki catchment, and (iv) prepared field-plan map (guide map) for further filed inventory work to collect GCPs from flooded and non-flooded part of the study domain (annex **A**).

From July, 2020 to October, 2020 the flood-prone area was frequently visited at overpass date of S-1 SAR satellite to collect GCPs from the flooded and non-flooded surface area following the field-plan map. These GCPs data were collected at the dates of 16 July 2020, 04 August 2020, 15 August 2020, 16 August 2020, 08 September 2020, 09 September 2020 and 21 September 2020. To match the S-1 image resolution the GCPs collected from the minimum flood inundated area of 10x10m. However, the GCPs for the non-flooded areas were collected at the edge of the flooded area and 10-30m (3 pixels far from edge of the flooded area). The flood extent of 09 September, 2020 was found large enough and hence used for validation of the flood hazard map that was extracted from S-1 image in this study.

From different LULC classes 433 GCPs were collected in December, 2020 which was one of the driest month in this study. These GCPs were covered six land cover classes of (forest, rainfed agriculture, irrigated land, grassland, and built-up and bare land) that used to train and validate the LULC classification algorithm using the S-2 optical satellite image (Table 3.3).

Table 3.3 GCPs collected from the field in December 2020

LULC	GCPs
Built-up	153
Rainfed	48
Grassland	111
Forest	51
Bareland	25
Irrigation	45
Sum	433

3.5 Methods

The JavaScript was used to implement an algorithm for the flood inundation mapping and LULC classification on the GEE Application Programming Interface (API) platform. The JavaScript used for flood inundation mapping was originally prepared by UN-SPIDER[7]. However, the script was customized to the current study for rapid and automatic flood inundation mapping by using the S-1 SAR dataset for the Akaki catchment.

In this study, two common methods and polarizations were compared for flood inundation mapping. These methods are (i) change detection (CD) and (ii) intensity-based histogram thresholding (HT). The major common tasks in both methods consist of collecting the S-1 SAR satellite image, pre-processing, detect the flooded pixel, refining the flood maps and exporting the result to google driver.

In table 3.4 the general overview of the methods followed and applied in this study was described. The steps followed dataset used, data source and detail activity was pronounced.

3.5.1 Image pre-process

The S-1 SAR image is stored on GEE after pre-processing with the Sentinel Application Platform (SNAP) tool. These applied pre-processing actions are thermal and border noise removal, radiometric calibration, orthorectification, georeferencing at the global level (Clement et al., 2017). In this study, speckle filtering was undertaken as additional pre-processing of S-1 SAR

[7] http://www.un-spider.org/advissupport/recommended-practices/recommended-practice-google-earth-engine-flood-mapping/step-by-step

image. Datum transformation was applied for the DEM obtained from EGII. The detail of the image pre-processing of S-1 SAR and DEM is presented in the following sub-sections.

Speckle noise is a common problem to be overcome before using the S-1 SAR dataset. It caused by random interface of signal backscatter from multiple rough land surface when combined in a single platform and collapsing the signal wave interface with small particle (Zhang et al., 2020). Various speckle noise filtering methods have been used in the literatures (Gouveia, et al. 2019; Yommy et. al. 2015; Liu, 2016). However, the selection of the method and window size to filter the speckle noise may result in information losses. In the S-1 SAR high signal backscatter variability is generated due to the solid materials, temporal vegetation situated in the flooded area.

In this study median statistical method was applied in small window size of 3x3 to minimize the effect of high signal backscatter variability and to protect information losses accordingly. This median filter method is not influenced by the extreme signal backscatter generated from the flooded surface (Bhatthttps et al. 2017; Andreoli and Yesou, 2007).

The coordinates of a features existing on the DEM, satellite image, global dataset and on the ground surface may vary due to their datum difference. The horizontal datum (reference) of the 10m DEM obtained from EGII was Adindan. However, the WGS 1984 was used for the satellite images, global dataset and local datasets (GCPs) that were collected from the field. Horizontal deviation was observed when the river segment digitized from Google Earth image (WGS 1984) overlaid on the DEM (Adindan datum). Therefore, it was found important to transfer the coordinate of the DEM to match the coordinate of the satellite dataset (S-1 SAR, S-2), GSW dataset collected from GEE and local dataset (GCPs) collected from the field. The local datum of the DEM (Adindan) was transformed into the global datum of the WGS 1984.

Table 3.4 General over flow of methods used in this study

Steps	Dataset	Data Sources	Activity
1. Pre-processing the satellite imageries and DEM	i. The S-1 SAR satellite image , ii. The S-2 optical satellite image iii. 10m resolution DEM	i. GEE for (S-1 and S-2) and, ii. EGII for DEM	i. Speckle filter was applied for (S-1). ii. Select the cloud free image, mosaic and band composition for (S-2). iii. Datum transformation for (DEM).
2. Flood inundation mapping using the method of (i) Change Detection (CD) and (ii) Histogram Thresholding (HT).	i. The VV, VH polarizations of S-1 SAR dataset that is acquired on 09 September, 2020. ii. Global Surface Water (GSW) dataset for permanent water body iii. Terrain slope.	i. GEE for S-1 and GSW ii. DEM for the terrain slope.	i. Band-math: - (Square Root of Normalized Image Difference) applied for the (CD) method. Applying threshold to detect the flood pixels, refine the flood maps using the terrain slope and mask the permanent water body. ii. Single image analysis for the HT method, apply threshold on the histogram of signal backscatter intensity of target image to differentiate the flooded and non-flooded (land surface), and mask permanent water body.
3. Validate the flood inundation maps.	i. The flood inundation maps generated ii. GCPs collected from the field on the overpass date of S-1.	i.Step-2 ii. Field inventory	i. Error matrix prepared for flood inundation maps generated in the step-2 using GCPs. From the matrix the, producer's, user's, overall accuracy, and kappa statistics coefficient were determined. ii. Select the best performed method and polarization used for flood mapping in Akaki catchment
4. Produce the time-series flood inundation maps by using the selected method and polarization in (step-3)	S-1 SAR dataset acquired from April to November of 2017 to 2020.	GEE	i. Generate the flood inundation map from April to November of 2017 to 2020 and determine the percentage of flooded area corresponding to the Akaki catchment size. ii. Frequency of flood occurrence based on the percentage of flood affected pixels.
5. Detect major flood affected roads in Addis Ababa city	Flood frequency occurrence map generated in step-4 and google earth image.	i.Step-4 ii. Google Earth image	Overlay the flood frequency map generated in step-4 on the Google Earth image to identify the flooded affected roads, and sub-city,
6. LULC classification	Cloud free S-2 optical satellite image acquired at the period of rainfed agriculture dominated (01 April, 2019 to 12 May, 2019) and irrigated agriculture dominated (01 December, 2018 to 01 March, 2019) in, 2019.	i. GEE ii. Field inventory	i. Train the classification algorithm by using GCPs obtained from Google Earth image and field inventory. ii. Validate the LULC map corresponding to GCPs collected from the field.
7. Flood hazard assessment .	The time series flood frequency occurrence map and the LULC map generated in (step-4) and (step-6).	Step-4 and Step-6	i. Determine flood affected LULC area.

3.6 Flood Detection

Rapid, automatic and accurate flood inundation mapping techniques is preferred to rapidly response for flood affected community and damage preventions (Muhadi et al., 2020; Yuan et al., 2019). However, all the methods used to generate flood inundation maps using S-1 SAR dataset are categorized as single and multi-temporal image analysis.

In this study, two different methods and polarizations of S-1 SAR are compared for flood inundation mapping. These methods are (i) histogram thresholding (HT) (single image analysis) and (ii) change detection (CD) (multi-temporal image analysis) by using VV and VH polarization of S-1 dataset. The detail of these methods are presented in the following sub-sections.

3.6.1 Histogram thresholding.

The histogram thresholding is a method that uses single S-1 image for flood inundation mapping. The method was built based on the common characteristics of S-1 signal backscatter intensity generated from the flooded and non-flooded surface. Low signal backscatter reflectance and dark imagining are obtained from the calm flooded surfaces (Bhatthttps et al., 2017). Therefore, the signal backscatter intensity histogram of S-1 SAR image is expected to contain two peaks (for the water bodies and for other land surfaces). The expected flood threshold value used to distinguishes the flooded and non-flooded surface is located inside the gorge of the two peaks (Hara et al., 2019). Then, the pixels with intensity less than the threshold are classified as the flooded pixels.

For this study, the threshold value obtained from the literatures was specified first (Ganji et al., 2019). Next the threshold value was adjusted based on the expert knowledge of the boundary between flooded and non-flooded area as recognized during the field observation on the date of the satellite overpass. Therefore, the flood threshold value was adjusted iteratively until acceptable accuracy is obtained and the flood map resembles what was observed in the field on one of the satellite overpass date (09-September-2020). The method was applied separately for co-polarization (VV) and cross-polarization (VH) of S-1 SAR. Then the flood maps generated from the two polarizations was compared using the performance indicators.

3.6.2 Change detection

The change detection is the second method evaluated in this study. The method uses multi-temporal satellite images which are acquired at the time of dry season (reference) and flooded season.

The applied steps and algorithm used to extract the flooded pixel are summarized as follow: -

- Select the reference image that contained minimum irregularity index (i) from candidate images collected from the driest period (January of 2017 to 2020).
- Estimate the Root of Normalized Image Difference (RNID) for the reference image (I1) and flooded image (I2) (equation 3.1).
- Apply threshold to cluster the flooded pixel from the RNID.
- Refine the flood inundation map via (i) binaries with the terrain slope, (ii) mask the permanent water bodies. See the detail for change detection method in the following sub-sections.

High signal backscatter variability is generated from the flooded surface due to non-fully submerged temporal vegetation, flood depth variability, water surface roughness due to wind effect, and solid materials existing inside the flood surface (Tsyganskaya et al., 2018**;** Schlaffer et al., 2015).

In this study, the root value on the RNID method is used to only detect the pixels that contained lower signal backscatter intensity than the dry (reference) image. Additionally, the high signal backscatter variability between the flooded and non-flooded surface is clear to visible on the RNID map which used to simplify identification of the flood threshold value. The equation of RNID reads: -

$$R = \left(\frac{I1-I2}{I1+I2}\right)^{0.5} \quad \text{.....3.1}$$

where: - R is the root of the normalized image difference, I1 is the signal backscatter intensity of the reference image, I2 is the signal backscatter intensity of the flooded (target) image.

This method was applied on the S-1 SAR image acquired on 09 September, 2020. In this study the reference image was selected as described in the following section.

3.6.2.1 Reference image

Reference image has a vital role in change detection method to obtain the optimal flooded pixels due to high signal backscatter intensity variable between the S-1 reference (dry) image and flooded image (Clement et al., 2017).

Two steps were followed to select the better reference image that can be used for flood inundation mapping for this study. These steps are:- first the dry season (January) images were selected as the candidate images and second, the image with the minimum value of the irregularity index (i) was selected (Hostache et al., 2012). January is the driest month without any flood incidence in the Akaki catchment. Therefore, the image acquired in January of 2017 to 2020 were identified as the candidate of the reference image. Next, the irregularity index (i) of the reference images was determined as the difference between 95% observed (referred) signal backscatter intensity of histogram and 5% observed signal backscatter intensity of histogram. The image that has the minimum value of irregularity index (i) was assumed free from flood incidence pixels.

In this study, two flood inundation maps were generated by using different reference images to evaluate the effect of reference image in flood map and, effect of acquiring the reference and flooded target image from different years. The first reference image was selected from all candidate images that contained minimum irregularity index (i). However, for the second reference image two possibility was established. These possibilities are first, the image contained minimum irregularity index was selected from the candidates of January (2020) reference image that acquired in the same year of target flooded image, the second reference image is selected from the candidates of January (2017 to 2019) that contained minimum irregularity index. These flood maps were generated using S-1 dataset acquired on 09 September, 2020. Therefore, the reference image effect in the accuracy of flood map was determined corresponding to GCPs collected on the overpass date of the satellite.

3.6.3 Terrain and permanent water body mask

Steep terrain slope cause a change in the direction of signal backscatter intensity (Long et al. 2014). The sensor depression angle less than the terrain slope generates layover and shadow on the radar sensor lead to generate false flood alarm in flood mapping (Zeng et al., 2020**;** Zhang et al., 2020; Clement et al., 2017). Therefore, the terrains slope masking should be used to discard

such false flood alarms that occurred in the S-1 image. In this study, the pixels were masked out if the terrain slope exceeds 2%.

The permanent water body was masked to obtain the actual flood which was generated by the rainfall. In this study, the water body that was detected and stayed for more than five months (January, February, March, November and December) were masked as permanent water body. Such permanent water body dataset was obtained from Global Surface Water (GSW) dataset.

Table 3.5 summarizes key characteristics of the histogram threshold and change detection method that was used to map the flood inundation in Aakaki catchment. These characteristics include required, method, limitation, strength and parameter of both methods.

Table 3.5 Summary of histogram threshold (HT) and change detection (CD) method

	Histogram Threshold (HT)	Change Detection (CD)
Requires	Single satellite image	Multi-temporal (dual) satellite images
	User involvement (field inventory) is required for the validation (optional).	User involvement (field inventory) is required for the validation (optional).
Method	Bimodal histogram is generated for the water surface and land surface area. The flood threshold value was found at the gorge of the bimodal histogram.	Applying band-math on the reference (dry) and flooded (target) image. However, the method was integrated with automatic threshold to cluster flooded pixels (Stephanie Long, 2014).
Limitation	**i.** It is susceptible to false positive flood alarms generated from feature sandy area, shadow, layover that have similar backscatter characteristics as the flooded surface (Schlaffer et al., 2015). **ii.** The bimodal histogram generated from very large land surface and small water surface pixels makes difficult to defining the flood threshold (Nakmuenwai, et al 2017).	**i.** Signal backscatter intensity may be affected by temporal land surface variability and observation angle between the reference and flooded image. **ii.** The reference image may affects the accuracy of flood inundation map.
Strength	**i**. The method is highly flexible, rapid and automatic to detect the flooded pixel for land and flooded surface is proportional. **ii**. The result not affected (dependent) by the temporal varying pre-signal backscatter intensity of the study area.	**i.** Only detect the changes obtained between the dry season (reference) image and the flooded season image to reduce effects of (double bounce, layover, shadow) on signal backscatter that generated from permanent features existed in both reference and flooded image (Li et al., 2018).
Required parameters	Target (flooded) image, flood threshold, permanent water body and terrain slope.	Reference image, target image, flood threshold, terrain slope and permanent water body.

3.6.4 Collection of Ground Control Points (GCPs)

The GCPs (reference) data collected used to train, calibrate and validate the algorithm applied for flood inundation mapping and LULC map detection from satellite dataset (Mohd Hasmadi and

Kamaruzam, 2008; Nkomeje, 2017). Various techniques are offered to determine minimum required sample size of (GCPs) that can be used to validate the maps generated from RS satellite dataset. For this study, the binomial distribution equation is used to determine the minimum required GCPs for accuracy assessment (Banko, 1998, Nkomeje, 2017) (equation 3.2).

$$N = \frac{Z^2(P)*(q)}{E^2} \quad \ldots\ldots\ldots\ldots\ldots\ldots\ldots\ldots\ldots\ldots\ldots\ldots \quad (3.2)$$

where: - N is the required sample size, Z = 2 (from the standard normal deviated of 1.96 for the 95% two-tail confidence level (CL) (Nkomeje, 2017), P is the expected accuracy (85% for this study), q is expected error (i.e. 100 – P = 15%), E is the allowable error from normal deviation.

Equation 3.2 resulted in 196 GCPs (sample) data for the accuracy assessment. However, the catchment size and number of land cover classes to be classified were not considered in the equation 3.2. Nevertheless, as a rule of thumb 50 to 100 GCPs were recommended per each land cover classes to validate the maps generated from satellite image (Nkomeje, 2017). In this study, 179 GCPs were collected from flooded surface and 54 GCPs were collected from the non-flooded surface to validate the flood inundation maps that generated on 09 September, 2020. Whereas, 434 GCPs were collected from different land cover class to validate the LULC map generated from S-2 optical satellite image. Therefore, the number of GCPs satisfied both the statistical requirement and the rules of thumb recommended based on previous works.

3.6.5 Accuracy Assessment.

The accuracy assessment is an important task to determine the quality of the maps generated from satellite dataset. Further use the satellite products map is determined by their level of accuracy. In this study, the error matrix was used to evaluate the accuracy of the flood inundation and LULC map. The matrix contains n x n (rows and columns) size, where n is the number of land cover classes. The column contains the GCPs that are from each land cover classes, and the row contain the classified data using the satellite image. The diagonal element in the matrix indicate the correctly classified pixels whereas, the non-diagonal element describes not-correctly classified pixels. Additionally, the matrix determined total number of GCPs collected in each land cover classes. The overall accuracy, producer’s accuracy, and user’s accuracy are determined. Additionally, the agreement between the land cover classes was determined by the statistical analysis of kappa coefficient.

Particularly, the overall accuracy and the kappa statistics coefficient are strong on determined the accuracy of classified maps. The overall accuracy is determined as the ratio of the sum of the diagonal elements divided by the total number GCPs (reference data). Whereas, the producer's accuracy is estimated as the ratio of correctly classified pixels of each LULC class to the total GCPs collected for the particular land cover classes. The omission error is the complement of producer's accuracy and determined as 100% minus the producer's accuracy. The user's accuracy is determined as the ratio of the correctly classified pixel and that total of pixels classified in particular class. The commission errors is determined as 100% minus the user's accuracy. All these accuracy terms described as a percentages.

The kappa statistic coefficient (k) is another method of accuracy assessment. It considers all the elements of the matrix. The method is referred to as the multivariate agreement between the land cover classes (Caprioli & Tarantino, 2001). It is used to evaluate how the classification well performed than randomly assigned value and it is a strongly measure than the simple percentile description (Nkomeje, 2017). It is stated as equation 3.3:-

$$k = \frac{\mathrm{Po}-\mathrm{Pe}}{1-\mathrm{Pe}} \quad \ldots\ldots 3.3$$

where: - Po is the proportion of observed agreement (overall accuracy), P_e is the proportion of randomly expected accuracy.

Pe is determined from the marginal element of the matrix which is the ratio of the sum of the diagonal element and the sum of total marginal elements. The marginal matrix elements arranged by sum of GCPs that collected in each land class obtained in row was multiplied by sum of GCPs that collected in each land class existed in the column. New marginal matrix that has equal size with original matrix was generated.

The kappa coefficient value is positioned between 0 and 1. The accuracy of the maps can be determined as k value < 0.00 is poor, 0.00 - 0.20 is slight, 0.20 - 0.40 is fair, 0.40 - 0.60 is tolerable, 0.60 - 0.80 is significant, 0. 80 - 1.00 is nearly perfect. The kappa coefficient increases when the chance agreement decrease and vice versa (Rwanga and Ndambuki, 2017; Nkomeje, 2017). .

For this study, the accuracy assessment was undertaken to compare different methods, and polarizations of the S-1 SAR images used for flood inundation mapping based on the overall accuracy and kappa statistics coefficient obtained from the error matrix. Additionally, the

reference image effect on the change detection method was evaluated corresponding to kappa coefficient and overall accuracy. Therefore, the method and polarization that resulted best performed accuracy (in terms of overall accuracy and kappa statistics coefficient) were selected for time-series flood inundation mapping as discussed in the following section.

3.7 Time-series flood inundation mapping and analysis

Flooding occurs over a certain time duration whereas, the satellite provides an instantaneous (snap shot) data of the flooded surface. However, the time-series satellite data can provide useful information to characterize the flood hazard (Martinis & Plank, 2018). In Akaki catchment flood commonly occurs from June to September. However, it might be stretched to another months occasionally (source:- personal communication with the local community situated in the flood-prone area).

The flood inundation maps were generated from April to November of (2017 to 2020) by using the selected method and polarization of the S-1 dataset. The flood frequency occurrence of each pixel was estimated to shown seasonal and inter-annual flood variation in Akaki catchment. The dynamics of flood was evaluated as increasing and decreasing the percentage of the flood extent corresponding to the Akaki catchment size.

3.7.1 Flood frequency occurrence

Frequency of flood occurrence determined by the repeatedly flood affected pixels when applying RS dataset in time-series analysis (Zhang et al., 2020). In this study, each flood affected pixels were categorized as rarely, sometimes, moderately, mostly and always affected based on the frequency of flood occurrence in time-series analysis. Different steps were followed to categorize the flood affected pixels in flood frequency occurrence classes.

These steps are (i) binary map was generated first with value of 1 indicating (flooded pixel) and 0 indicating (non-flooded pixel) for flood inundation maps detected at satellite overpass date from April to November of 2017 to 2020, (ii) flood frequency occurrence is estimated by aggregating (through addition) of binary maps for each individual months of (April to November) over the four years 2017 to 2020, (iii) the monthly flood inundation was aggregated for each year of 2017, 2018, 2019 and 2020 to determine annual flood occurrence frequency, (vi) the four years flood frequency occurrence maps were aggregated for inter-annual analysis, (v) Threshold value was applied to

categorize the flood affected pixels into five flood frequency occurrence classes of (rare, sometimes, moderately, mostly and always).

For this study, pixel was categorized in to "always affected" class when the flood occurrence exceed 90% of time, whereas, it was categorized ''mostly affected" pixels when flood frequency is from 60% to 90%. Pixels affected by flood from 40% to 60% were categorized as moderately affected. The pixels that were categorized from 10 to 40% of the time and less than 10% of the time were categorized as "sometimes affected" and "rarely affected pixels respectively.

3.7.2 Flood affected roads and sub-cities in Addis Ababa city

The author of this study, was witnessed many flooded streets in the Addis Ababa city during extreme rainfall[8]. The weak performance of the city's drainage system is mentioned as the major reasons for the occurrences of this street flood. However, such flood usually last for few minutes to hours and occasionally few days. As result the sniping shot of S-1 SAR satellite per twelve days interval may miss such flood affected roads. However, the time-series of flood inundation maps can capture such flood affected roads when the analysis period is long as it is the case in this study i.e. four years of (2017 to 2020). Then, the time-series flood inundation map were overlapped in the google earth image to differentiate such affected roads.

Additionally, the most flood affected sub-cities of Addis Ababa city were identified based on the time-series flood maps over the analysis period of this study. The time-series flood frequency map were overplayed on the administrative boundaries shapefile of Addis Ababa's sub-cities. Therefore, for each sub-city the flood inundated area and frequency of flood occurrence was analyzed.

3.8 Flood affected LULC classes

Recurrence occurrence of flood can potentially damage properties, affect mobility, and result in different level of impacts (Rose, et al. 2014). In this study, the flood hazard for each land use land cover (LULC) class of the study area was determined by (i) mapping the LULC class, (ii) estimate the percentage area of each LULC class that is affected by flood.

The LULC map of this study area was classified using pre-processed S-2 level-2A dataset. Pre-processed S-2 level-2A (SL2A) that contained bottom atmosphere reflectance (BOA) dataset

[8] https://www.tobiatube247.com/article-read.php?a=1313

implemented to detect the LULC classes[9]. Orthorectified with UTM/WGS84 projection and atmospherically corrected by using S-2-toolbox were loaded in the GEE (Verde et al., 2020). Therefore, to match the datum reference of S-2 dataset with the flood inundation maps and GCPs collected from different LULC classes the default geometry reference was used. The cloud free satellite image (with less than two percent cloud cover) was collected for the analysis. Two image scene covered the Akaki catchment was mosaicked, the satellite image was clipped using the boundary map of Akaki catchment and band-composition was applied to visually differentiate the land cover classes.

In this study, supervised classification method was implemented for LULC classification. The method is flexible based on the expert's knowledge and the GCPs collected from the field used to train and calibrate the algorithm. The expert's knowledge of the study area was fully implemented in classification. The algorithm was calibrated until the classified image reasonably satisfied based on the ground truth to obtained optimal result. In GEE different machine learning algorithms can be chosen to apply supervised classification based on the collected GCPs. Among these algorithms Classification And Regression Tree (CART), NaiveBayes and Support Vector machine (SVM) algorithms have been commonly applied (Nguyen et al., 2020).

To compare these machine learning algorithms error matrix used corresponding to GCPs applied to train and calibrate the algorithm in the GEE, figure 3.4(a). For train and calibrate the algorithm 1608 GCPs were implement. From these 467 GCPs collected from the field exclude the water body GCPs were used for accuracy assessment.

[9] https://sentinel.esa.int/web/sentinel/user-guides/sentinel-2-msi/processing-levels/level-2

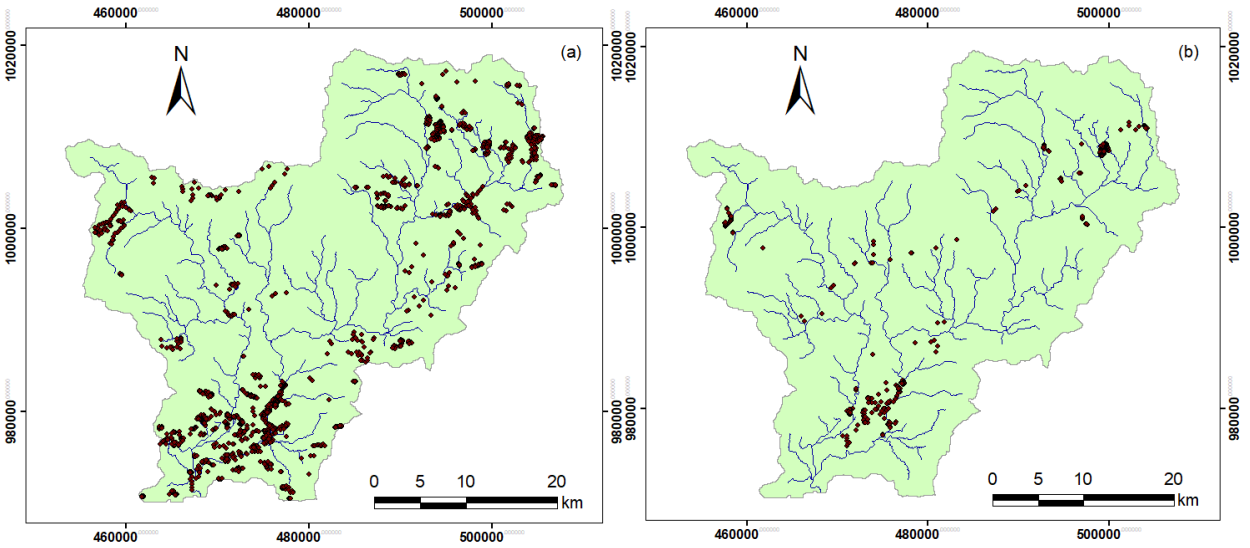

Figure 3.4 Spatially distributed GCPs used for calibration (a) and validation (b)

There are both rainfed and irrigated cropping in this study area. Hence, two S-2 optical satellite image that were acquired from two different seasons (dry and wet) were selected to capture both cropping practice in the Akaki catchment. These seasons were classified as non-rainfed agriculture activity and irrigated agriculture activity. Seven land cover classes (bult-up, rainfed agriculture, irrigated agriculture, bare land, mixed forest, grassland and water bodies) are observed dominantly in the catchment. In this study, the resident, industry, commercial, asphalt, and rocky land cover area were categorized as urban (built-up) area due to their similar hydrological response (run-off generation). Additionally, temporal vegetation, dense forest, small shrub land were categorized in the mixed forest land cover classes.

The irrigation (non-rainfed) agriculture activity occur from November to March (personal communication with the farmer at the downstream of Akaki catchment). Whereas, the rainfed agriculture occur from April to November. Three steps were followed to generate LULC map that obtained for the two unalike seasons. These steps are (i) all LULC classes were detected from the satellite image acquired in the time period of (01 April, 2019 to 12 May, 2019) (rainfed agriculture dominated season) that the cloud free image was obtained and for irrigated agriculture dominated season the time period (01 December, 2018 to 01 March, 2019) used to acquire the cloud free satellite image, (ii) select the rainfed land, built-up area, bareland, grassland, mixed forest, water body of the study area were identified for the LULC that were generated from the wet season (01 April, 2019 to 12 May, 2019) and the irrigated land was extracted from the dry season second time

period of (01 December, 2018 to 01 March, 2019), (iii) merge the maps in step i and step ii through map overlay analysis.

Flood affected LULC classes were determined based on the percentage of flood inundated area in the past four years. The time series flood inundation maps from April to November of 2017 to 2020 overlaid on the LULC map to estimate the extent and occurrence of flood frequency in each LULC classes.

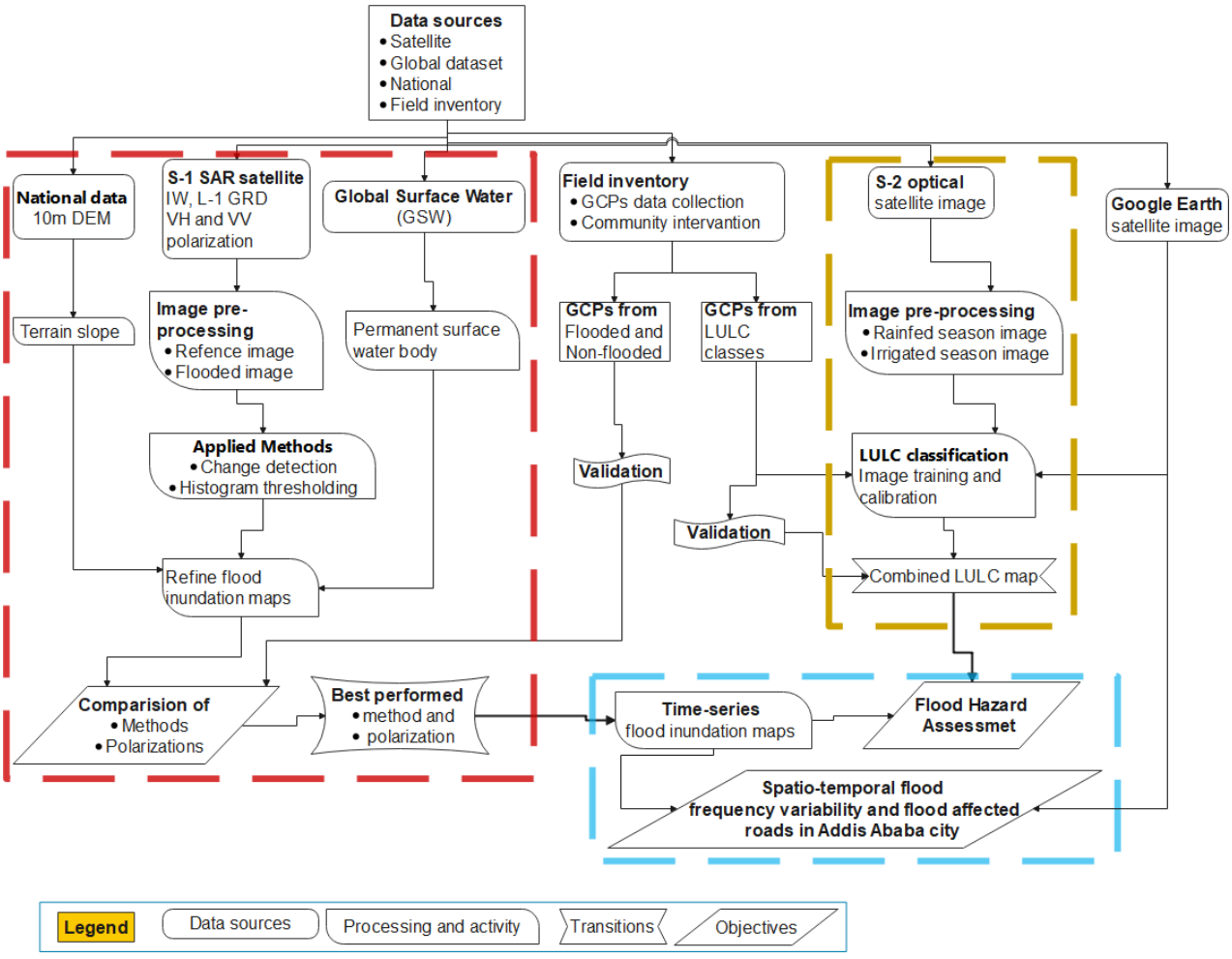

Figure 3.5 General workflow of the thesis

4 RESULT AND DISCUSSION

In this section, the results are presented and interpreted for (i) the accuracy of the methods and polarizations of the S-1 SAR used for flood inundation mapping (ii) the time-series flood frequency occurrence map and dynamics of flood extent (temporal and spatial) generated in Akaki catchment from April to November of (2017 to 2020) (iii) flood affected major roads in Addis Ababa city and the land use land cover classes.

4.1 Accuracy assessment for the flood inundation maps

Flood inundation map can be useful for flood risk management only if the accuracy level is in acceptable range. For this study, error matrix was used to determine the accuracy of the flood inundation maps. The overall accuracy and kappa statistics coefficient were used to compare the accuracy of flood inundation maps produced by Histogram Thresholding (HT) and Change Detection (CD) methods via using co-polarization (VV) and cross-polarization (VH) of the S-1 SAR dataset. The comparison was applied for the flood maps of 09 September, 2020 using GCPs that were collected from the field at the same date of satellite overpass.

4.1.1 Histogram Thresholding

Histogram thresholding method requires single satellite image for flood inundation mapping. The signal backscatter intensity characteristics of the S-1 SAR is dependent on the type of polarization, hence the flood threshold value is varied (figure 4.1). The VV polarization is characterized by high signal backscatter intensity due to low incidence angle than VH polarization. For this study, the optimal flood threshold value to distinguish the flooded and the non-flooded surface was determined via trial and error (manually) until the value of overall accuracy and kappa statistics coefficient reach acceptable range. Hereafter, -15 and -21 dB of flood optimal threshold value were attained for the VV and VH polarizations respectively.

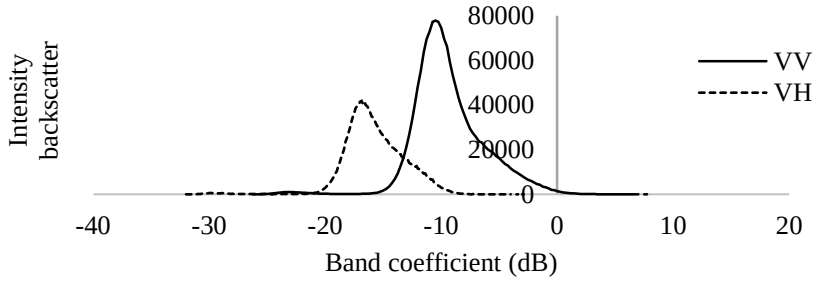

Figure 4.1 Histograms of the S-1's SAR satellite image for the date of 09 September, 2020

The user's accuracy was obtained as 87.7% from flooded and 90.7% from non-flooded surface. High commission error was observed in the flooded surface due to the GCPs collected near the shore, fully saturated soil (low-depth flood) produced high signal backscatter intensity as the non-flooded surface. Whereas, from 69.01% to 96.91% the producer's accuracy was ranged (Table 4.1) and high omission error was observed in the non-flooded surface. The overall accuracy was 88% obtained from total randomly collected GCPs and the kappa statistics coefficient that describe the general agreement between classified classes was 71 %. Generally, the accuracy of flood inundation map detected using VH polarization is enough good.

Table 4.1 Error matrix of the flood inundation map which is produced for September 09, 2020, by using the VH polarization and the method of histogram thresholding.

	Reference data (GCPs)				
	Flooded	Non-flooded	∑	User's accuracy	Commission error
Flooded	157	22	179	87.7%	12.3%
Non-flooded	5	49	54	90.7%	9.3%
∑	162	71	233		
Producer's accuracy	96.91	69.01			
Omission error	3.09	30.99			

Overall accuracy is 88% and 71 % of the kappa coefficient was attained.

The error matrix of the flood inundation map detected by using VV polarization was not shown here for the sake of brevity. However, the accuracy of flood inundation map detected by using VV polarization was lower than the accuracy of flood map detected by using VH polarization. The overall accuracy obtained from VV polarization is 79% and the kappa statistics coefficient is only 53.8% (annex **C)**. Generally, the accuracy is moderate.

4.1.2 Change detection

The change detection method requires two satellite image (reference and flooded image) to detect the flooded area. For this study area, January is one of the fully driest months without flood incidence. Therefore, ten candidate images were found as reference from 2017 to 2020 and single reference image was selected based the irregularity index (i) which is as the image contained minimum difference between 95% observed histogram of signal backscatter intensity and 5% observed histogram of signal backscatter intensity. Table 4.2 shows that January 06, 2019 image contained minimum irregularity index (i) and hence selected as reference image.

Table 4.2 Signal backscatter irregularity (i) index for the study area

Year	2017		2018		2019			2020		
Day-Month	04-01	28-01	11-01	23-01	06-01	18-01	30-01	01-01	13-01	25-01
95%	56572	57683	57683	57728	55501	56286	55187	56429	57154	56165
5%	1949	1655	1655	1613	2197	2220	1576	637	903	1292
95% - 5% (i)	54623	56029	56029	56115	**53304**	54066	53611	55792	56251	54873

In this study, to show the reference image effect on the accuracy level two flood inundation maps were produced by using two different reference images and compared. These reference images are (i) January 06, 2019 (which is identified by minimum irregularity index (i) from all the candidate images) and the (ii) January 25, 2020 (it is contained minimum irregularity index from the same year as the flood image of (September 09, 2020). Note, each reference images have the same parameters (i.e. polarization, orbit pass direction and resolution, incidence) as the flood (target) image. The flood inundation maps generated by using different reference image are shown in annex **D**.

For the flood inundation map detected by using January 06, 2019 reference image only 5.29% average commission error is observed. The producer's accuracy was ranged from 85% to 98.3%. However, slight confusion as 15% of omission error was observed in the non-flooded surface class. The overall accuracy is 95% which determines the accuracy of flood map corresponding to total randomly collected GCPs. The kappa statistics coefficient is 86% determined the agreements between classified classes. Generally, the accuracy of flood inundation maps using VH polarization is very good (Table 4.3).

Table 4.3 Error matrix of the flood inundation map of September 09, 2020, by using the method of change detection and January 06, 2019 as reference image, VH polarization

	Reference data (GCPs)				
Classified	Flooded	Non-flooded	∑	User's accuracy	Commission error
Flooded	170	9	179	94.97%	5.03%
Non-flooded	3	51	54	94.4%	5.56%
∑	173	60	233		
Producer's accuracy	98.3%	85%			
Omission error	1.7%	15%			

The Overall accuracy is 95% and the Kappa coefficient is 86%.

For the January 25, 2020 reference image the overall accuracy is 94% and the kappa statistics coefficient is 84.4%. This indicates that the accuracy of the flood inundation map still good (Table 4.4). However, it is slightly low than the accuracy of the flood inundation map generated by using the reference image of January 06, 2019. It designates that the selection of the reference based on minimum irregularity index has only slight effect on the accuracy flood inundation maps and the same time period (year) used to acquire the reference image and the flood image is an optional.

Table 4.4 Error matrix of the flood inundation map which is produced from September 09, 2020, by using the method of change detection using the January 25, 2020 reference image, VH polarization.

	Reference data (GCPs)				
Classified	(1)	(2)	∑	User's accuracy	Commission error
Flooded (1)	172	7	179	96.1%	3.9%
Non-flooded (2)	6	48	54	88.9%	11.1%
∑	178	55	233		
Producer's accuracy	96.6%	87.3%			
Omission error	3.4%	12.7%			

The overall accuracy is 94% and the kappa statistics coefficient is 84.4%.

The error matrix of the flood inundation map produced by using VV polarization of September 09, 2020 flooded image and using January 25, 2020 reference image is presented in the annex (**E**). For this, the overall accuracy is 86.7% and the kappa coefficient is 67.5%. This indicates that the VV polarization performed less accurately detect the flooded pixel than the VH polarization.

4.1.2.1 Flood threshold value

Figure 4.2 shows the histogram of root of normalized image difference (RNID) between the signal backscatter intensity of the reference image (06 January, 2019) and the flooded image (09 September, 2020). Note, in the method the pixels only contained low signal backscatter intensity than the reference image is detected. The histogram is smooth at the starting of the curve detected from the smooth land surface which is characterized as low signal backscatter intensity then the reference image. However, high difference (heterogeneity) of the curve is clearly shown from the flooded surface due to the flood depth variability, non-submerged temporal vegetation, and solid materials situated in the flooded surface. Therefore, the flood threshold value was fixed at the starting point of signal variability observed in the histogram. The accuracy of the applied method was evaluated by the flooded image of September 09, 2020 and the threshold value is 0.019.

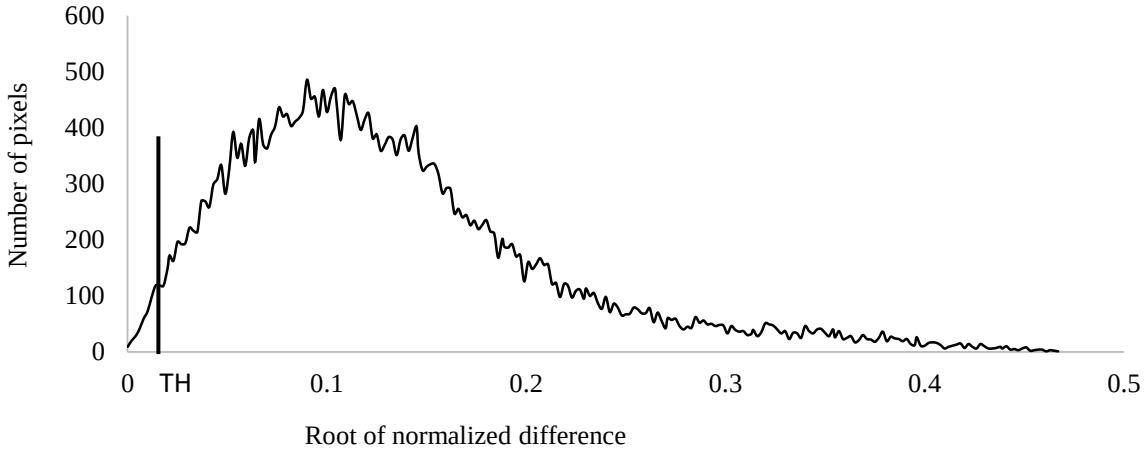

Figure 4.2 Histogram of the root of normalized image difference of the signal backscatter for January 06, 2019 (reference image) and September 09, 2020 (flooded image). The flooded pixel was located to the right-hand side from the Threshold (TH) value.

Figure 4.3(a) and figure 4.3(b) show the flood inundation maps of the Akaki catchment produced by the method of (i) change detection and (ii) histogram thresholding respectively by using VH polarization which performed better accuracy than VV polarization. Widespread of false flood alarms are shown on the North East (NE) part of the catchment figure 4.3 (b)) indicating the limitation of histogram thresholding method in detecting floods. The NE part of the catchment is extensive agricultural activity and the soil was not fully moist without impound of water as observed during field visit. The flooded area detected by the method of histogram thresholding was 5.17 times larger than the flooded area detected by the method of change detection.

Overall, based on the accuracy assessment presented so far the histogram thresholding method and VV polarization has significant limitation for flood inundation mapping in Akaki catchment. Therefore, the change detection method and VH polarization were selected to produce the time series flood inundation maps from 2017 to 2020 as described in the following section.

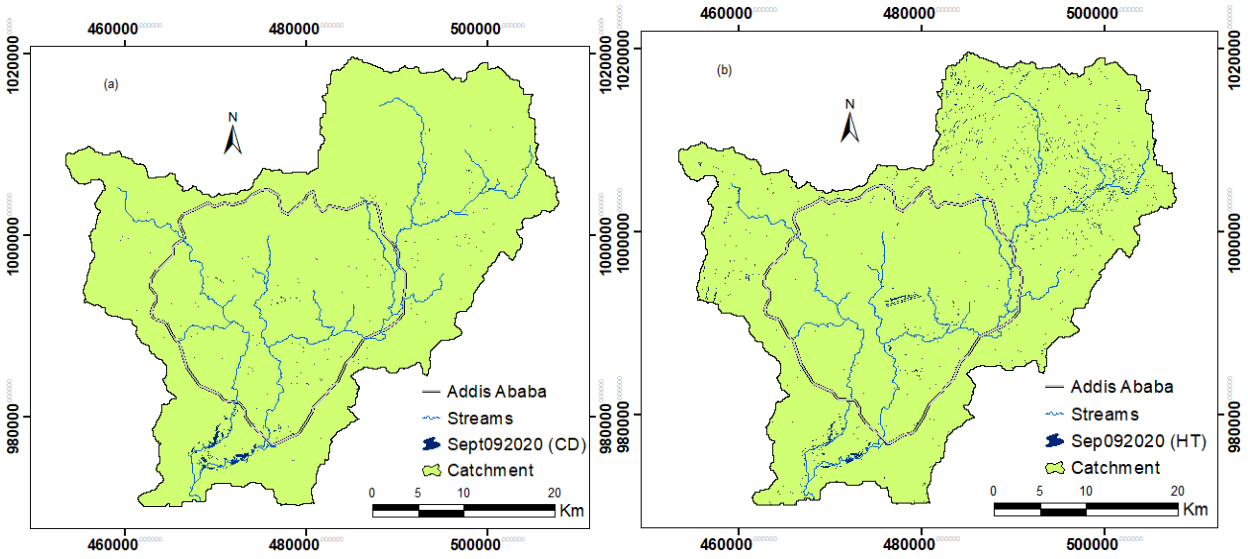

Figure 4.3 September 09, 2020 flood inundation maps generated by using the method of change detection (a) and histogram thresholding (b), using VH polarization

4.2 Time series flood analysis

In this section, the time-series of flood inundation maps generated from April to November of (2017 to 2020) by using change detection method, VH polarization and January, 06 2019 reference image were analyzed.

Figure 4.4 show the temporal flood extent variability detected in Akaki catchment of 2017 and 2018. The 2018 flood extent was mostly higher than the 2017. However, there are some exceptions in May, July, September and Octobers were detected. In 2017 maximum flood was obtained as late as the 2018 month's that observed the maximum inundated area. It inundated as 0.27% of the Akaki catchment size on October 19, 2017. The maximum extent of the flood in that was detected on 22 July, 2018 as 0.62% of Akaki catchment size.

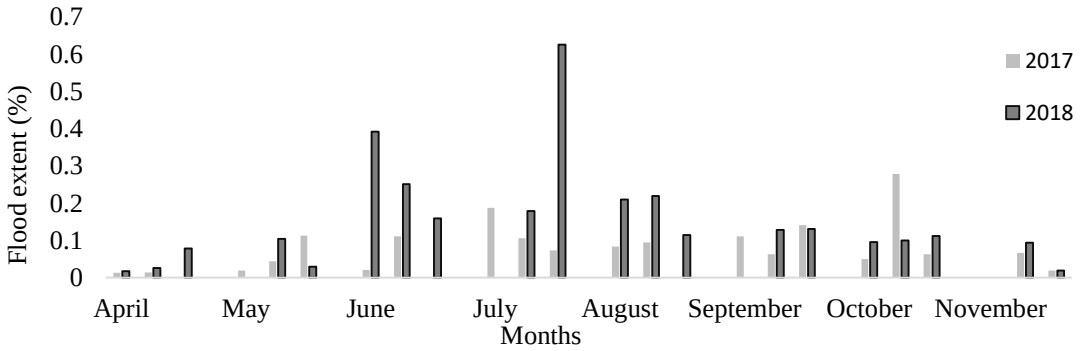

Figure 4.4 Flood extent in 2017 and 2018 determined as percent of the Akaki catchment size.

The 2019 and 2020 flood extent variability was shown in figure 4.5. The flood extent detected from April to middle July of 2019 was dominated than 2020. However, from the end of July to October 2020 high flood extent was generated in Akaki catchment than the 2019. On 23 July, 2020 and 09 September, 2020 large flood inundated area were detected as 0.26% and 0.24% respectively of Akaki catchment size. But, in 10 August, 2019 maximum flood extent was inundate 0.118% of Akaki catchment size.

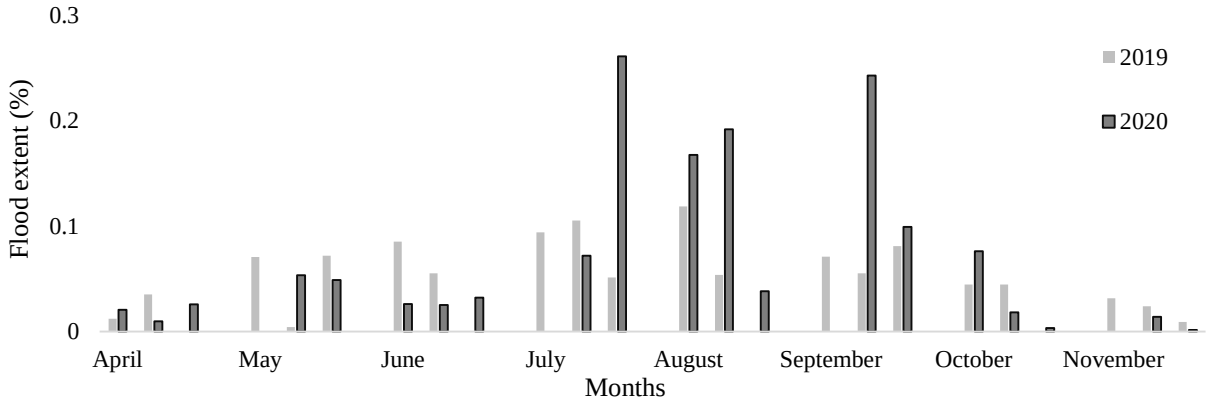

Figure 4.5 Flood extent in 2019 and 2020 determined as percent of the Akaki catchment size

Flood extent in Akaki catchment show large monthly and inter-annual variation from 2017 to 2020 (figure 4.6). From April it start to inundate the catchment and receded in the November. However, high flood extent variation observed from June to October and low flood extent variability observed in April, May and November.

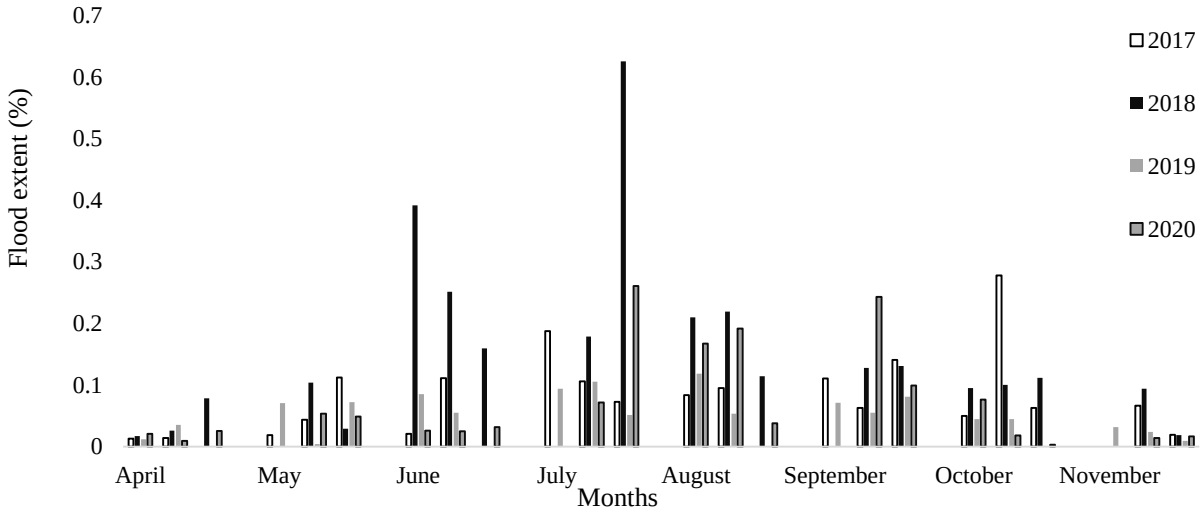

Figure 4.6 Flood extent from 2017 to 2020 as determined percentage of the Akaki catchment

In figure 4.7 show the sum of flooded inundated area detected from April to November of (2017 to 2020). In the maximum summation of flood extent is obtained in July as 1.88% of Akaki catchment size. However, from April to July the summation of flood extent was raised and high variability was observed. However, the summation of flood inundated area declined from August to recede in November and the variability was slight in this season.

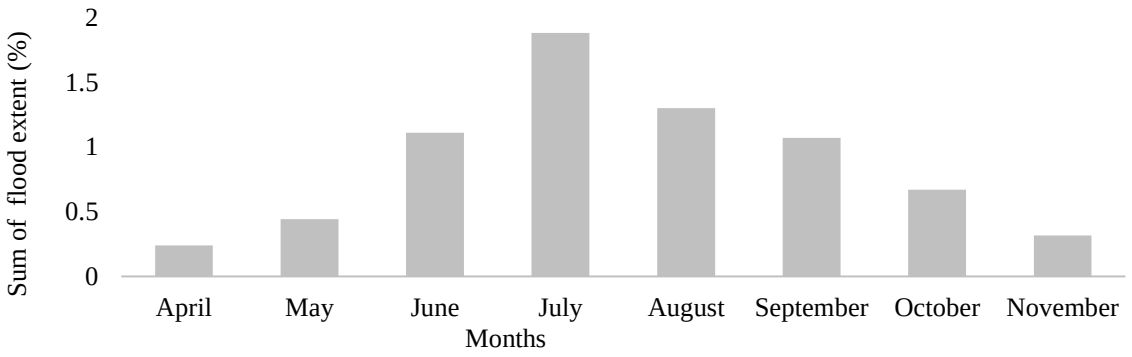

Figure 4.7 Summation of flood extent from 2017 to 2020 determined as percentage of Akaki catchment

4.2.1 Monthly flood frequency analysis

The occurrence of flood in Akaki catchment is categorized in to five frequency classes for the 8 months of 2017 to 2020 (figure 4.8). These flood frequency occurrence classes are rare, sometimes, moderate, mostly and always as indicated in the method section of this thesis. In all months (April to November) most part of the catchment area was affected by flooding as rarely and/or sometimes occurred. In April 96.03% of the flooded area is categorized as rare and sometimes affected area. However, high flood frequency classes (moderate, mostly and always) affected area was observed in July, August and September.

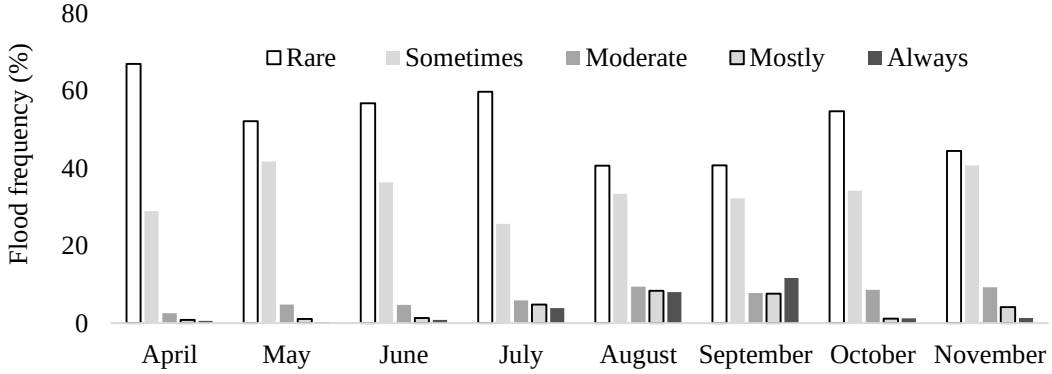

Figure 4.8 Monthly flood frequency occurrence in Akaki catchment from (2017 -2020)

4.2.2 Monthly flood inundation maps

The extent and frequency of flood for the entire Akaki catchment were discussed in the previous sub-sections. However, the downstream part of the catchment was widely affected by riverine and pluvial flooding. Therefore, this area was selected as interest of domain to provide detail information on the spatiotemporal flood variability from April to November of 2017 to 2020.

In figure 4.9 (a) shows the flood frequency occurrence map classified in different frequency classes for April of (2017 to 2020). In the big Akaki riverside, small flood pockets were observed at the downstream of railway station. Similarly, small inundated area were detected at the most downstream part of little Akaki riverside which is situated close to Aba Samuel reservoir. However, the flood inundation area was slightly increased and expand to the upstream in the May's (figure 4.9 (b)). Along the big Akaki riverside new flood pockets was detected slightly upstream of the flood pockets that emerged in April. New flood pockets (not observed in April) were also detected in the May at the most downstream part of little Akaki river. The floods of April and May have rare frequency that is expected considering the rainfall occurrence is low in these months.

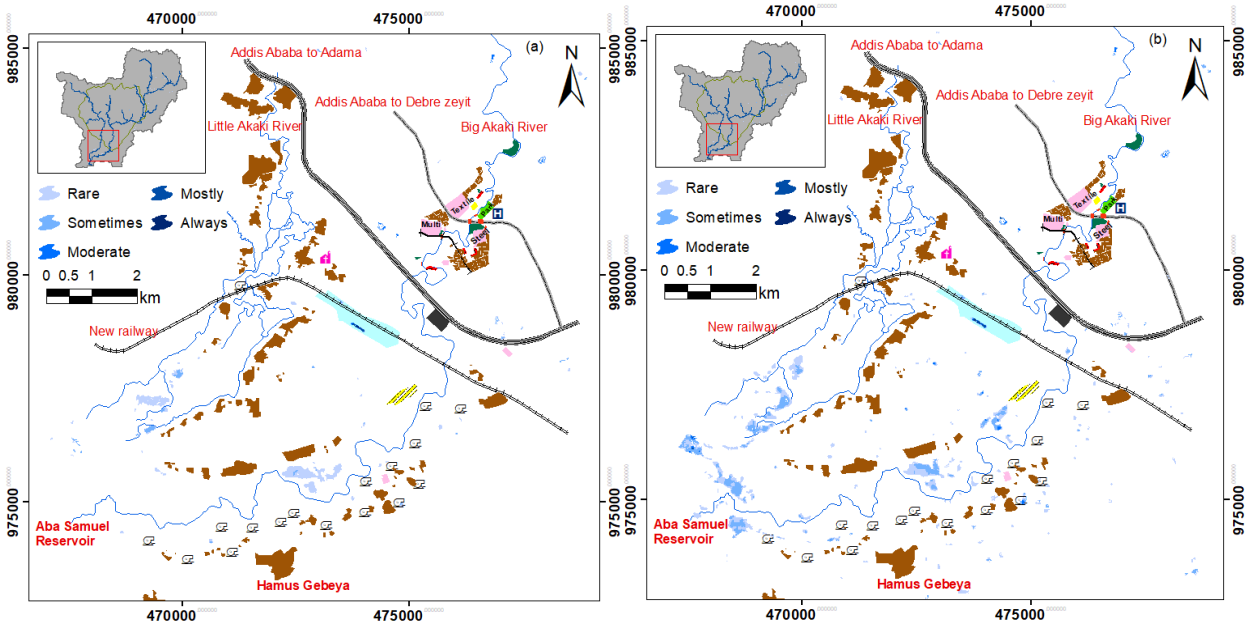

Figure 4.9 Flood frequency map generated for April (a) and May (b) of (2017 to 2020)

In figure 4.10 (a) the flood frequency map is shown for June of (2017 to 2020). The existing flood pockets increased in size whereas several flood pockets were merged in June due to pluvial flood around the area between the big and little Akaki river.

In the big Akaki riverside several flood clusters with large extent were captured stretching from the Kilinto prison to Aba Samuel reservoir. The isolated flooded area were started to be connected to form extensive flooded area along the little Akaki riverside. It indicates as small additional flooded area detected inside the villages which are situated downstream of new railway. The flood has rare to moderate occurrence in June.

In July, the extent of flood was extremely increased compared to that of June figure 4.10(b)). In the big Akaki riverside isolated flood pockets were connected. In this month the flood was extended from the upstream of Tirunesh Beijing Hospital (TBH) which is near to the dense forest to the Aba Samuel reservoir. Additionally, high pluvial flood was detected between the big and little Akaki riverside. In July, the flood occurred very frequently as (mostly and always) in the area that is situated at the downstream of Kilinto prison. However, flood occurrence is rare and sometimes for the area that is situated upstream of Kilinto prison. Along the little Akaki riverside the flood extended from the area around new railway (rare frequency) to the Aba Samuel reservoir (high frequency of occurrence). The resident near the new railway and their livestock are affected by the flood which is rarely occurring in July.

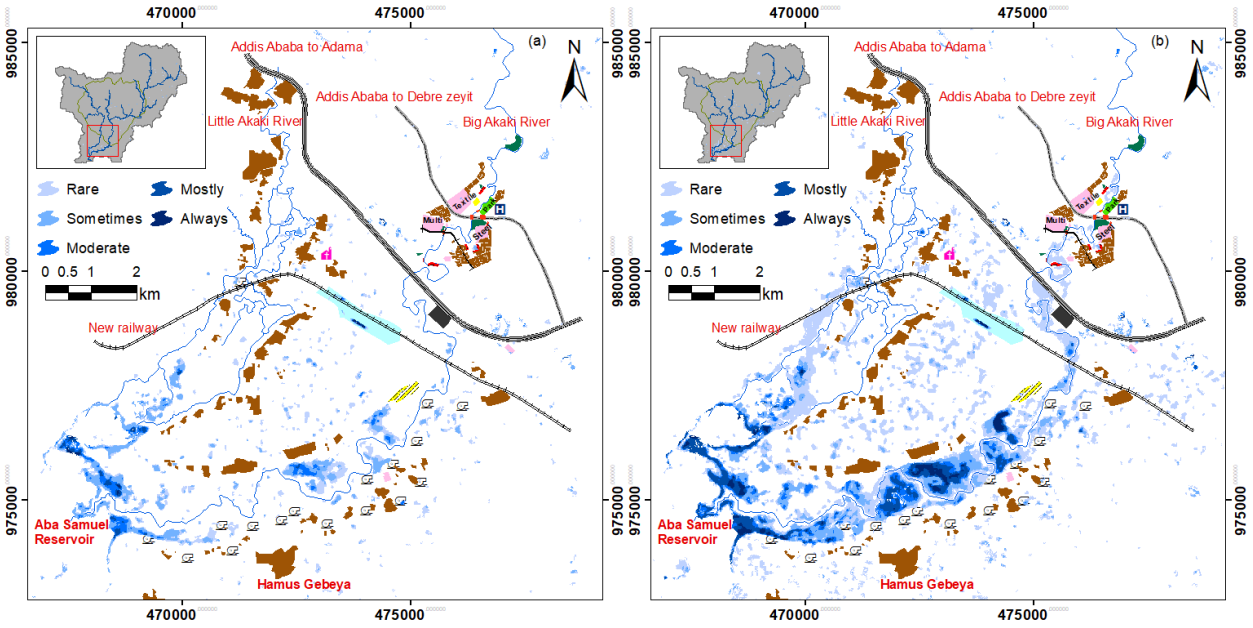

Figure 4.10 Flood frequency map generated for June (a) and July (b) of (2017 to 2020)

In figure 4.11 (a) August flood frequency is shown from (2017 to 2020). The riverine and pluvial flood observed in July was shrunk. Along the big Akaki riverside the flood was stretched from

upstream of TBH to the downstream of Aba Samuel reservoir. However, small flood discontinuity was observed near to Kilinto prison. High frequency (mostly and always) flood occurrence was observed at the inside meandering section of the river which is situated downstream of rail station along the big Akaki riverside. Along the little Akaki riverside rare flood affected area was detected at the upstream of new railway. However, high frequently flood affected area observed at most downstream situated close to Aba Samuel reservoir.

The September flood frequency map generated from 2017 to 2020 was shown in figure 4.11 (b)). The pluvial flood observed in the previous month was withdrew. High frequently flood affected area extended from railway station to the downstream along the big Akaki river side until Aba Samuel reservoir. However, at the upstream of new railway large cluster isolated flood pockets were detected. In the little Akaki riverside which is situated downstream of railway new railway rare and sometimes floods were occur. However, high frequently flood affected area as (mostly and always) occurred at the most downstream close to Aba Samuel reservoir.

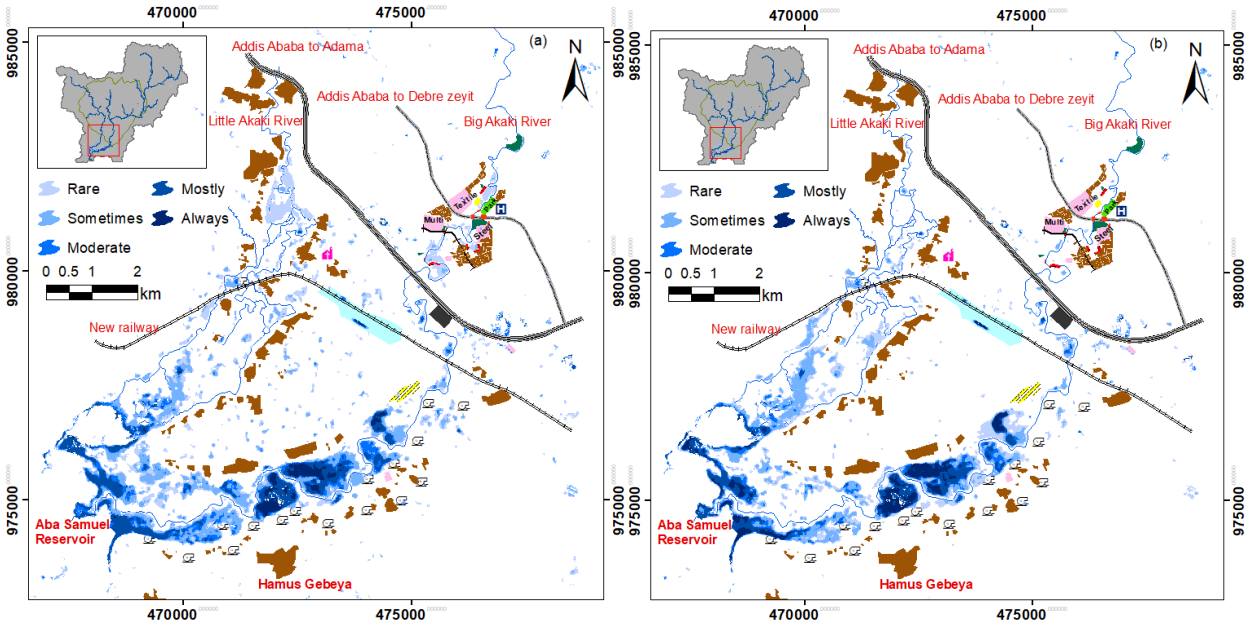

Figure 4.11 Flood frequency map generated for August (a) and September (b) from 2017-2020

In figure 4.12 (a) October flood frequency map is shown from (2017 to 2020). In this month the riverine and pluvial extent of flood were shrunk in both big and little Akaki riverside. This indicates that no new flood was generated and the existing flood was prolonged from the last month Large clustered high flood frequency was detected at the downstream of railways station inside

river meandering sections along the big Akaki riverside. In the little Akaki riverside which is upstream of new railway rare isolated flood pockets were detected and moderate flood affected area observed close to Aba Samuel reservoir.

The flooded period in Akaki catchment was receded in November as shown (figure 4.12 (b)). Only small isolated flood pockets that prolonged from October month is detected at the meandering section of the big Akaki river situated to Hamus Gebeya. Along little Akaki river rare isolated flooded area were detected at the beginning of November that the flood prolonged from October. Such flood were situated at the upstream of new railway and moderate floods detected at the most downstream situated close to Aba Samuel reservoir.

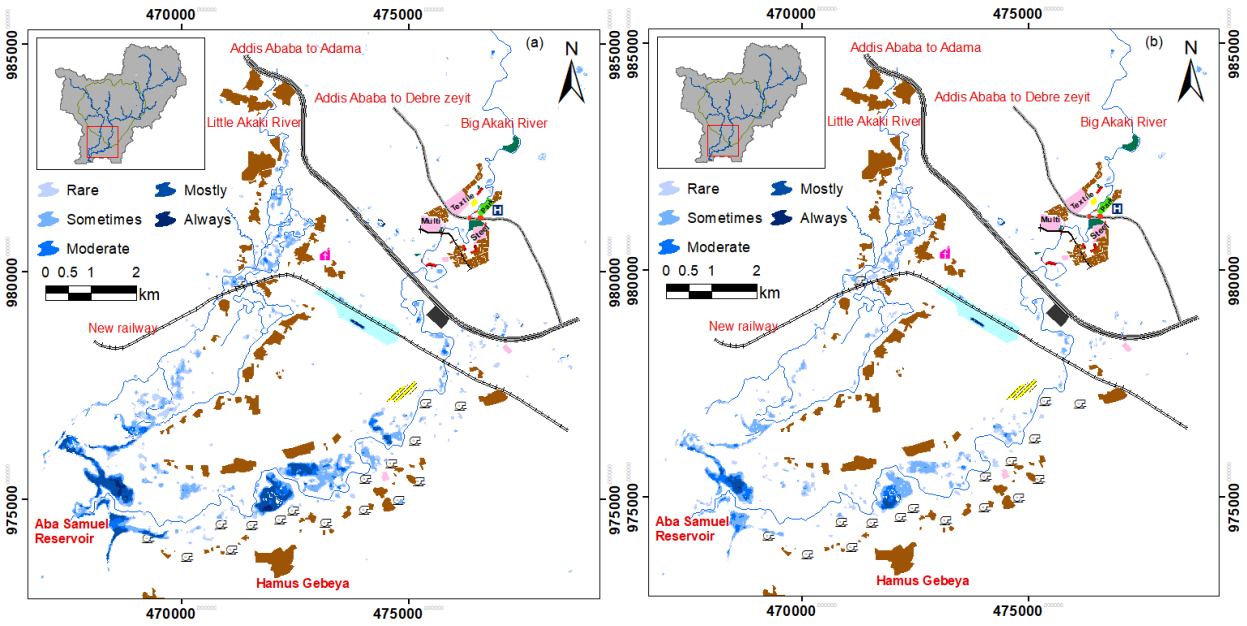

Figure 4.12 Flood frequency maps generated for October (a) and November (b) of (2017-2020)

4.2.3 Annual flood frequency analysis

In figure 4.13 show the annual flood frequency occurrence classes determined in Akaki catchment for 2017, 2018, 2019 and 2020. The frequency classes were assigned by categorizing occurrence of the flood in to five classes. The figure shows that high frequency classes was contained less than 1% of the total flooded area, whereas from 46% to 65% of the flooded area was categorized in rare flood affected area.

This suggested that managing these flood areas is not easy due to difficulty to predict the rare floods. Most new dry area was inundated and merged in 2018 and 2020 and inter annual flood variability in Akaki catchment was observed.

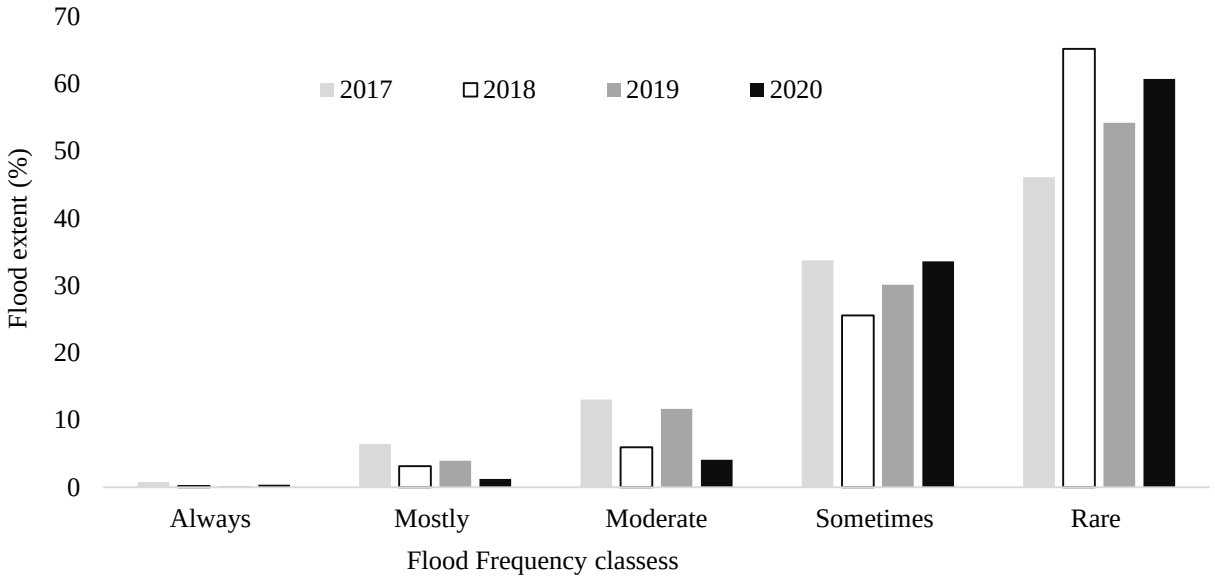

Figure 4.13 Yearly flood frequency occurrence in Akaki catchment from (2017 -2020). Annual flood inundation maps

4.2.4 Annual flood inundation maps

In this section discussed annual flood frequency map generated in Akaki catchment from 2017 to 2020. Figure 4.14 (a) shows flood frequency map generated from April to November in 2017. Along the big Akaki riverside rare to moderate flood affected area extended from expressway (Addis Ababa to Adama) to Aba Samuel reservoir. However, the area at the upstream of the expressway did not experience with widespread flooding. No pluvial flood was detected in the area situated between the big and little Akaki riverside. Small and isolated flood pockets were detected along the little Akaki riverside. Generally, in 2017 the rare to moderate flood affected area was dominated. However, at the most downstream which is situated close to Aba Samuel reservoir high frequent occurrence of flood (always) was observed.

In 2018, the maximum flood inundated area was detected from in Akaki catchment (figure 4.14 (b)). Therefore, the extent of flood is dramatically increased as compared with the 2017's and new dry area were submerges as flood.

This indicated that the area situated between TBH and Kilinto prison which is not inundated in 2017 was inundated in 2018. In the big Akaki riverside the flood was stretched from upstream of TBH which is situated to dense forest to the downstream of Aba Samuel reservoir.

The pluvial flood were widespread in 2018 covering the floodplain that is situated between the big and little Akaki rive and another dry area was covering with flood which is not inundated in 2017. However, these pluvial flood was categorized as occurring rare and sometimes affected area. Along the little Akaki riverside the flood started from expressway and then stretched to the downstream until Aba Samuel reservoir.

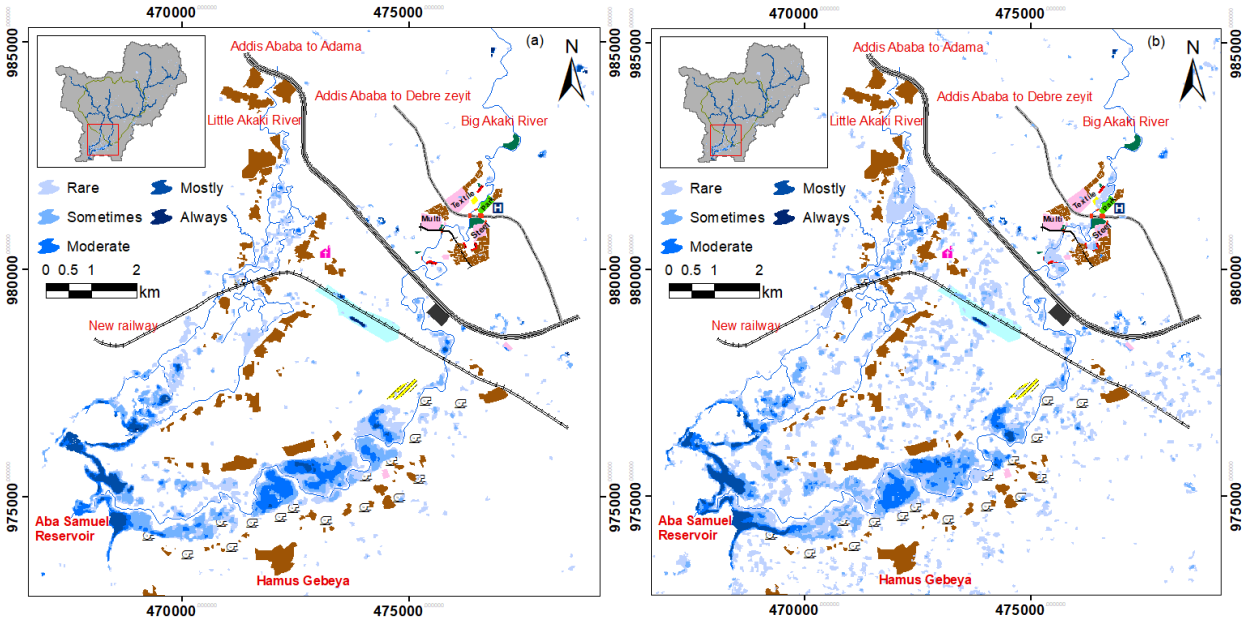

Figure 4.14 Flood frequency maps of 2017 (a) and 2018 (b)

The 2019, limited to relatively small extent shown in figure 4.15 (a). In the big Akaki riverside the flood was not extended to the upstream of new railway. It covered only that parts situated between new railway and Aba Samuel reservoir. However, flood extent extremely small and concentrating at the most downstream part of the little Akaki river side which is situated near to Aba Samuel reservoir. In this year from rare to moderate frequently flood affected area was dominated.

Figure 4.15 (b)) shows the flood frequency map generated in Akaki catchment, 2020. The extent of flood that detected in 2019 is stretched to the upstream from new railway until dense forest situated at the upstream of TBH along the big Akaki riverside. Along the little Akaki riverside the flood affected area observed from the villages situated near to new railway and then stretched to

the Aba Samuel reservoir. And, the pluvial flood and new dry area not inundated in 2019 was inundated in flood period of 2020. Affected flood inundated area was highly observed as rare and moderately frequency classes.

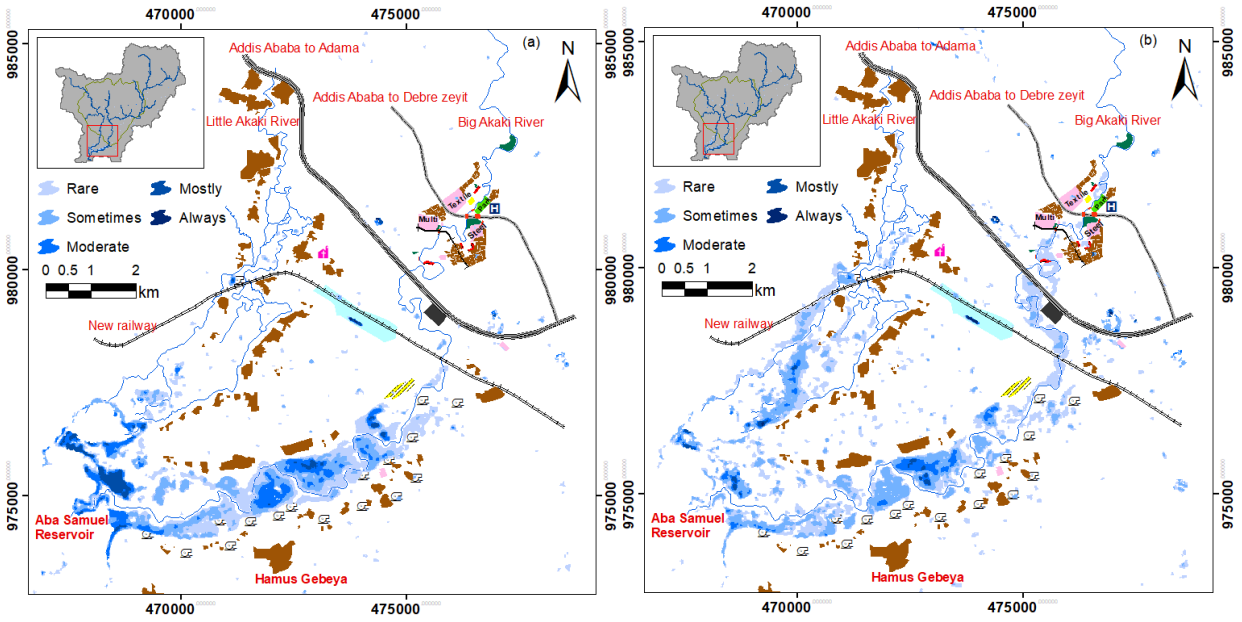

Figure 4.15 Flood inundation maps classified based on the frequency classes of the 2019 (a) and 2020 (b)

The flood frequency generated over the four years analysis period from (April to November) of (2017 to 2020) is shown in figure 4.16. Over this analysis period 80 S-1 satellite image was acquired in this study area. In four years flood period most flood inundated area was observed at the downstream of expressway (Addis Ababa to Adama). The villages situated at the downstream such expressway were encircled with flood and the community mobility and their livestock were highly affected by these floods. The water pumps shown in the map are used to pump drinking water to the upstream city was suggesting that early flood can cause damage. Most part of the flooded area was categorized as rarely occurred whereas at the meandering section of the river which is situated at the downstream of railway station in the big Akaki river side was affected by high flood frequency class (moderately and sometimes)

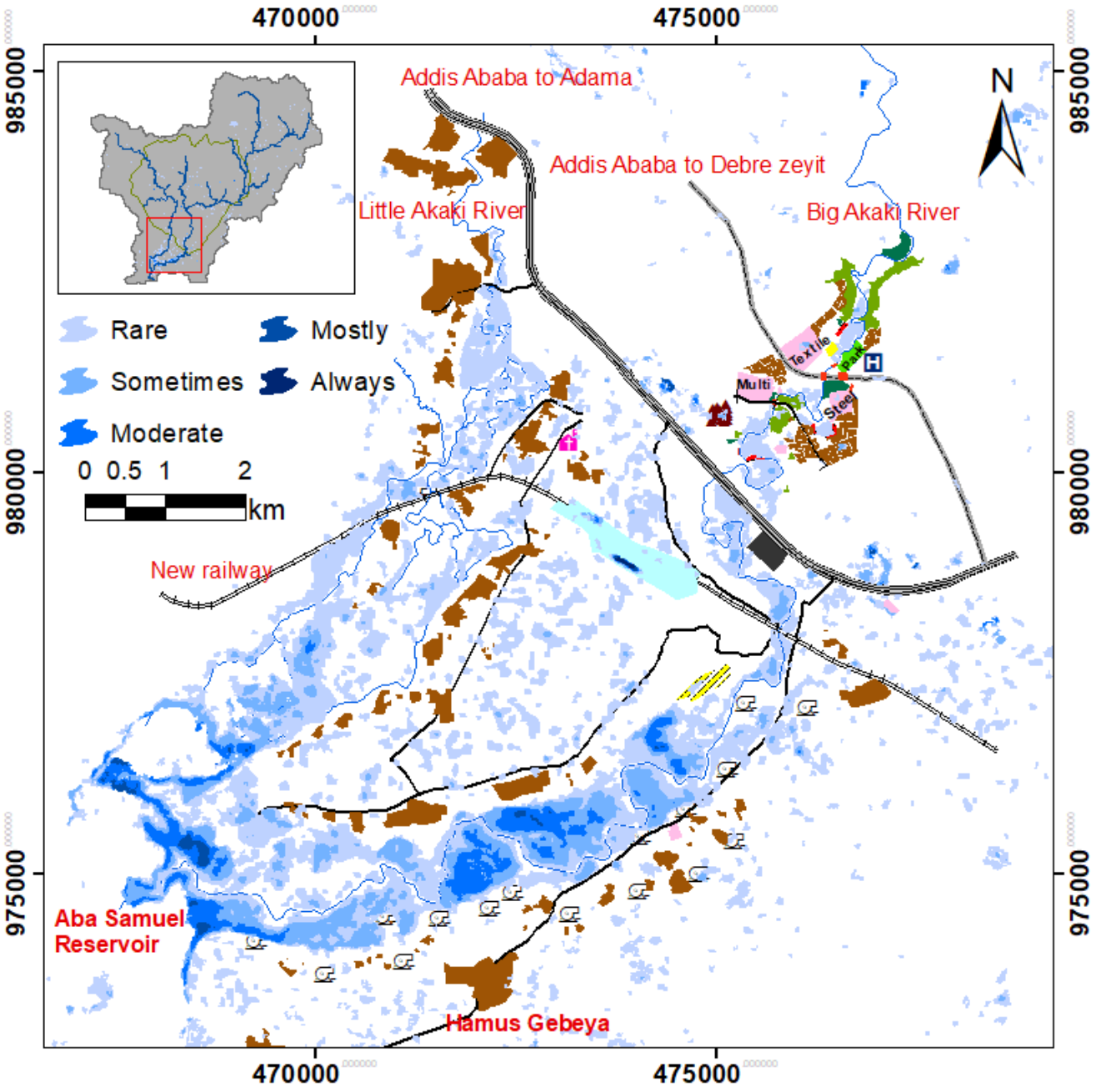

Figure 4.16 Flood inundation and frequency map at the downstream part of the Akaki catchment generated from April to November of (2017 to 2020)

4.3 Roads affected with flood in Addis Ababa city

In the past four years, residents observed that extreme flood event have been disturbing the traffics and human activity in the different part of the Addis Ababa city. The flood was caused by the extreme rainfall event and inadequate capacity of the drainage line of the city. Figure 4.17 shows main roads conveying flood water and disturbing the traffics activity.

Figure 4.17 June 13,2018 flood affected roads the Addis Ababa City due to extreme rainfall image source: - https://www.tobiatube247.com/article-read.php?a=1313 and https://www.ethiogrio.com/site/news/55564-flash-floods-kill-5-in-addis-ababa.html)

Satellite image capture snapshot of the flood image over interval of several days (e.g. 12 days for Sentinel-1 SAR) in Akaki catchment. As a result not all flood event are captured by the satellite. However, the flood maps generated from satellite image provide useful information when multi-temporal images are analyzed. The time series flood inundation maps which are generated from 2017 to 2020 displayed some of the roads which are affected by flood. These flooded roads were differentiated by overlapping the time series flood inundation maps over Google earth image. As an example floods was detected from Megenagna to Gurd Shola road figure 4.18(A) and from Mebrat Hail Lebu to Jemo 1 figure 4.18(B). See additional on annex (**H**).Informal discussion with resident near these roads revealed that the satellite image capture a real flood threat.

Figure 4.18 Roads affected by flood along Megenagna to Gurd Shola (A) and Lebu Mebrat Hail to Jemo 1 road (B)

The Addis Ababa city consists of ten sub-city (Akakai Kality, Nifas Silk Lafto, Bole, Kirkos, Kolfe Keranio, Lideta, Addis Ketema, Arada, Yeka and Gulele).

Several communities were interviewed from different parts of the city to validate the flooded roads detected by S-1 dataset (figure 4.19). These roads which were validated for the presence of flood threat area labeled as (A to G). However, the flood affected not only these labeled roads but, also many more. The detail of flooded affected road is presented in annex (**H**). Overall, the validation confirmed that the remote sensing image captured that affected flood roads in Addis Ababa city.

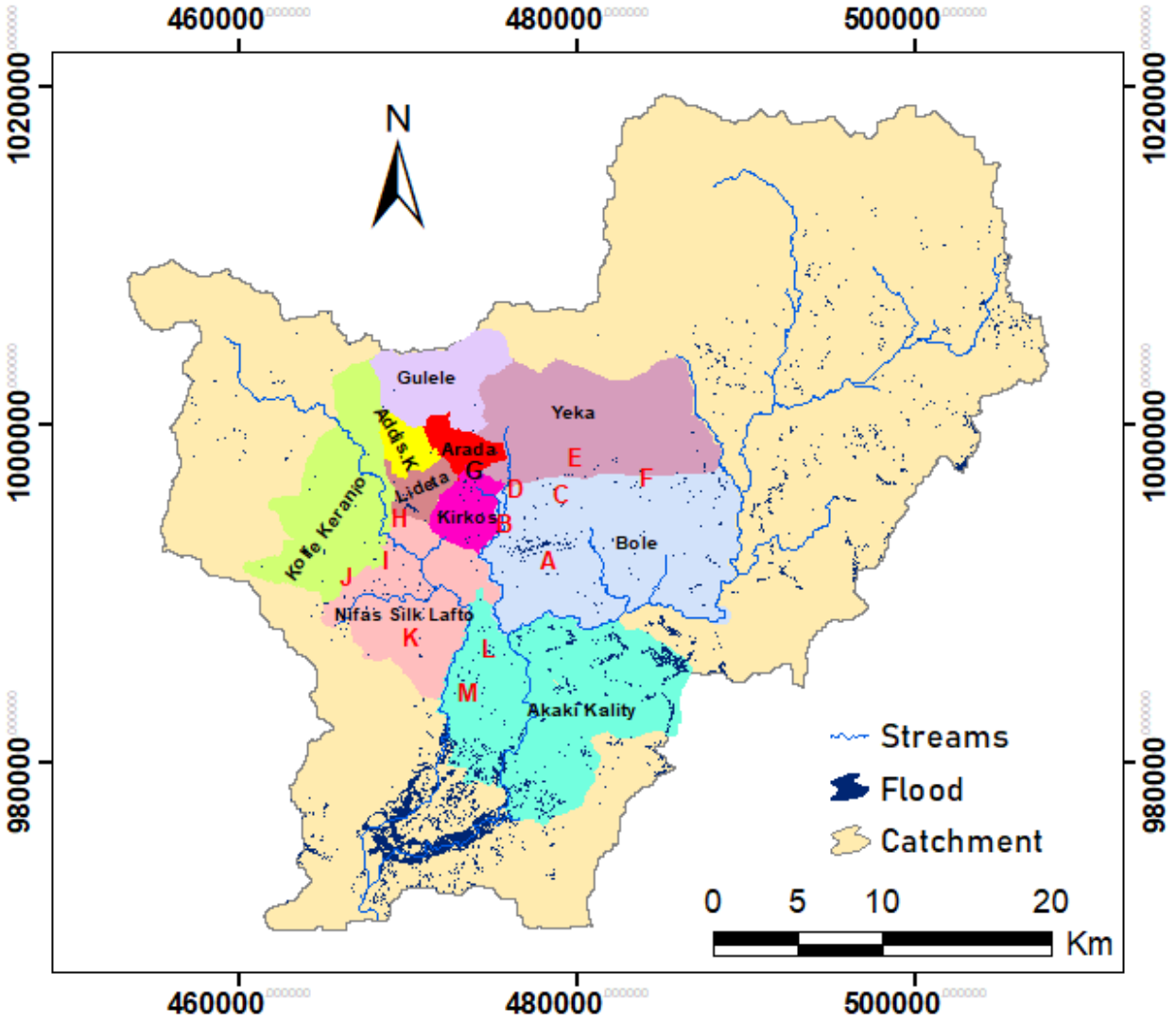

Figure 4.19 Flood inundated area in Akaki catchment over the four years of (2017 to 2020). The label in capital letter indicate some roads affected by flood and sub-city boundaries shown.

The Akaki Kality and Bole sub-cities are the most affected in terms of flood inundated area detected from 2017 to 2020. In Akaki kality 803.46 ha is inundated with 86.3% of the flood area representing rarely occurring flooded.

However, small part of (Addis Ketema, Arada and Gulele) were rarely affected by flood. These sub-cities were characterized by dense populated area with busy roads. This, even the rare flood event that cause substantial impact. Moderate flood frequency was observed in the Nifas Silk Lafto, Lideta, Yerka, Kirkos and Kolfe Keranio sub cities. Mostly and always occurring flood occure only in Akaki Kality, Bole and Nifas Silk Laft (Table 4.5).

Table 4.5 Flooded area that is detected in Addis Ababa's sub-city from (2017 to 2020)

	Flooded area (ha) in each frequency classes					
Sub-city	Rarely	Sometimes	Moderately	Mostly	Always	**Total**
Addis Ketema	2	0.19	0	0	0	2.19
Arada	2.18	0	0	0	0	2.18
Gulele	4.54	0.25	0	0	0	4.79
Kolfe Keranio	16.5	2.25	0.29	0	0	19.04
Kirkos	20.5	1.7	0	0	0	22.2
Yeka	21.12	2.27	0	0	0	23.39
Lideta	29.67	3.94	0.58	1.43	0	35.62
Nifas Silk Lafto	51.63	6.35	0.53	0.59	0.44	59.54
Bole	170	28.09	3.29	0.78	0.24	202.4
Akaki Kality	693.24	101.63	6.59	1.73	0.27	803.46

4.4 Flood affected Land Use Land Cover (LULC) class

In figure 4.20 shows the LULC map of the Akaki catchment generated from S-2 satellite image acquired in 2019. The upstream and central part of the catchment that consisted the Addis Ababa city is dominated by urban land cover. The urban area are contained the resident, commercial, industry, asphalt roads and rock land covered. The irrigated land use is dominated at the downstream of the catchment along both big and little Akaki riverside. The irrigated land is stretched from upstream of TBH near to the dense forest to Aba Samuel reservoir in the big Akaki riverside. However, from expressway to Aba Samuel reservoir high irrigated activity is there along little Akaki river and the area situated between the two rivers. And, urban agricultures used irrigated by using small streams in Addis Ababa city was detected.

From the NE to SE part of the catchment the rainfed agriculture land use is dominated. And, high forest area observed at the north boundary of the catchment which is situated to the Entoto Mountain. At the NE between reservoirs of (Legedadhi) and Sendafa small town the grassland cover is detected.

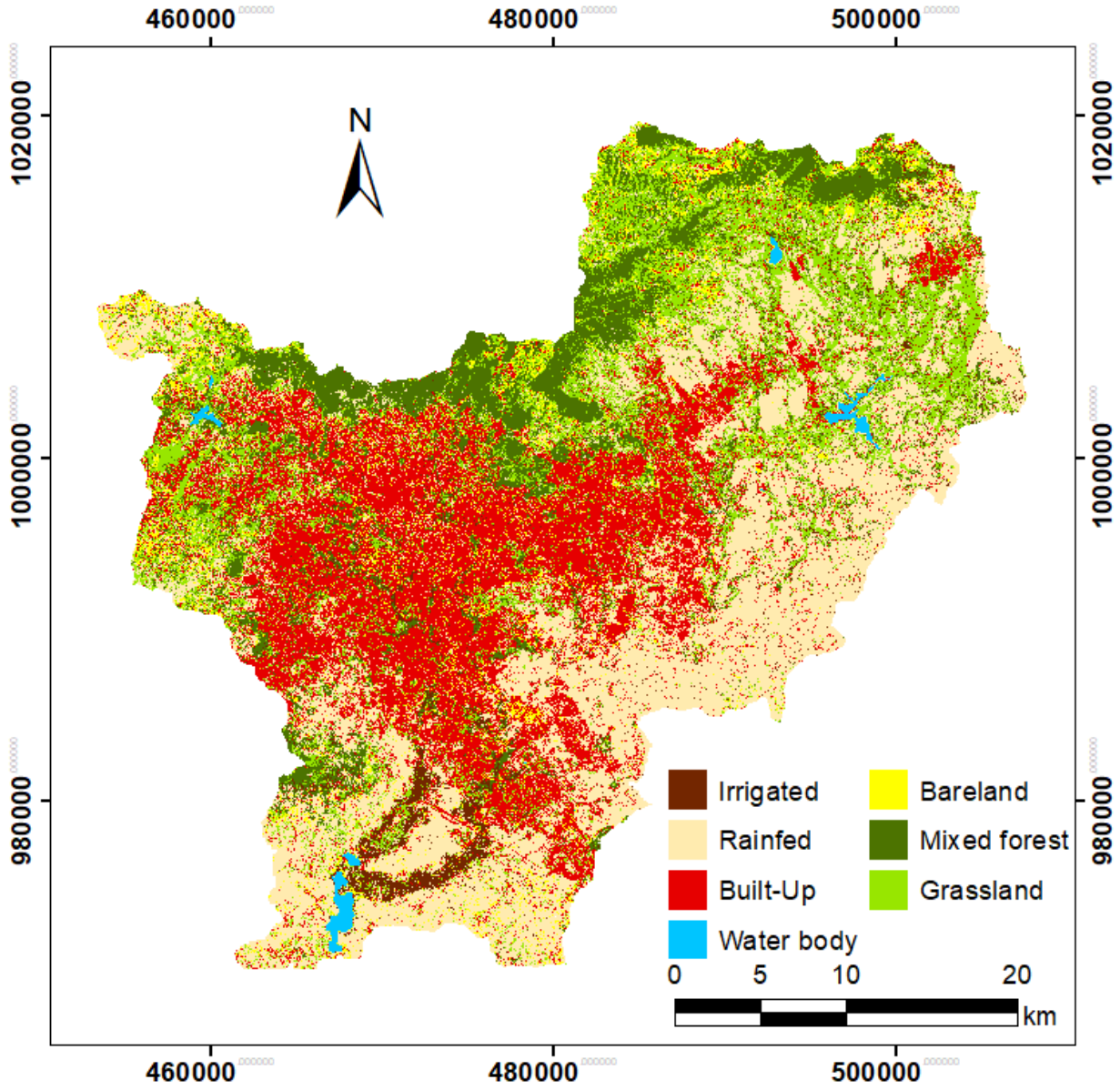

Figure 4.20 LULC map of the Akaki catchment

The rainfed agricultural and urban land cover are dominated in Akaki catchment. These land cover class contained 50034Ha (34%) and 37616 Ha (25.78%) of the Akaki catchment area respectively. However, another land cover class still cover large part of the catchment as 40.82 %. All land cover classes were affected by the flood that detected in the past four years of 2017 to 2020. However, the irrigated land is most highly affected land use class since 1057.05(ha) (21.28%) was inundated by the flood. Personal communication with the farmer situated at the downstream indicated the agriculture lead to produce only once a year and the flooding forced them to harvest early in response to unexpected early flood.

The urban area is the second most affected area with inundation covering of 544.11ha (1.44%) and this led to generate high flooding problems in Akaki catchment (Table 4.6).

Table 4.6 LULC classes in percent (%) of Akaki catchment size, and flood inundated area (ha) detected from (2017 to 2020) in each land covers and percentage (%) of the land cover

	Land Use Land Cover (LULC)		Flood Inundation	
LULC	Area (ha)	(%) of Akaki catchment	Area (ha)	Inundated (%) of the LULC area
Rainfed Agriculture	50034	33.98	208.53	0.42
Urban Area	37616	25.55	544.11	1.44
Bare land	8217	5.58	147.99	1.8
Forest Area	19247	13.07	73.31	0.38
Grassland	26277	17.85	281.69	1.07
Irrigated	4965	3.37	1057.05	21.28
Water Body	869	0.59		

4.4.1 Accuracy assessment

The error matrix is used to determine the accuracy of the LULC map corresponding to GCPs collected from the field. Use the dry season image did not satisfactory to capture on the rainfed agriculture land whereas the wet season image did not capture the irrigated land. Therefore, the rain season image and dry season image were merged to get better accuracy. The produce's accuracy ranging from 75% to 100% and high confusion observed in the rainfed agriculture land detected as urban. The user's accuracy was ranged from 84% to 100% since, little confusion was observed between the bare land and urban land cover class. The overall accuracy is 0.93% that determined the accuracy of LULC corresponding to randomly collect total GCPs. The kappa statistics coefficient that used determined the agreements between the LULCs is 0.91 (table 4.7). Overall, the accuracy of LULC map is very good.

Table 4.7 Error matrix derived for 2019 classified LULC map of the Akaki catchment.

	Reference Data							
Classified data	Built-up	Rainfed	Grassland	Forest	Water	Bare land	Irrigated	User's Accuracy
Built-up	142	8	3	0	0	0	0	93%
Rainfed	0	45	3	0	0	0	0	94%
Grassland	1	4	106	0	0	0	0	95%
Forest	0	0	3	48	0	0	0	94%
Water	0	0	0	0	34	0	0	100
Bare land	4	0	0	0	0	21	0	84%
Irrigatated	0	3	1	0	0	0	41	91%
Producer's Accuracy	97%	75%	91%	100%	100%	100%	100%	

4.5 Discussion

In both methods of change detection and histogram thresholding better accuracy was obtained when applied the VH polarization than the VV polarization data in flood inundation mapping. The VV polarization that has low incidence angle than the VH polarization was generate high signal backscatter intensity as the land surface from small depth flooded area. Hence, the flood that has small depth including pluvial flood was not detected in the VV polarization lead to underestimate flood affected area than the VH polarization similar to Clement et al., (2017) what was obtained. However, better accuracy were obtained in VV polarization since the same area were missed with the S-2 dataset that used to validate the S-1 data in flood mapping. This is the evidence as the secondary dataset introduce error which is not produced in the S-1 dataset and troubles to compare the studies result that were applied various dataset in the validation. Therefore, in this study, actual GCPs collected from the field at the date of satellite overpass to reduce the secondary error introduced during validation. In this study, significant difference in flood inundated area was perceived while applied VV and VH polarization data using change detection method. From the VV polarization data 511.37 ha of flood was detected whereas 256.23 ha of flooded area detected by the VH polarization data. This indicates that the VV polarization can penetrate through sparse soil and submerged area due to low incidence angle than the VH polarization to generate dark on the S-1 image as the flooded surface (Bayik et al., 2018; Gumma et al., 2020). During field visit at the date of satellite overpass the area that was dominated with farm activity and excavated for constructions were detected as flooded area in VV polarization. The overall accuracy of 95 % and 86.7 % obtained since VH and VV polarization data used respectively in the change detection method, whereas the kappa coefficients are 0.86 and 0.67. Significance difference was transpired which is 19% in the kappa coefficient than the overall accuracy due to competence of the agreement between the flooded and non-flooded area.

The change detection method was better in flood detection than histogram thresholding method in both VV and VH polarization data. In change detection method optimal overall accuracy is 95% and the kappa statistics coefficient 0.86 obtained whereas, in histogram thresholding method 88% overall accuracy and 0.71 kappa statistics coefficient during VH polarization data was used separately. This indicates that significance difference was witnessed between the kappa coefficient which is 15% distort in the agreement between the flooded and non-flooded surface. Widespread and random false flood affected area was shown on the North East (NE) part of the catchment

when applying histogram thresholding method. The sandy soil area and the agricultural land were not fully moist without impound of water was observed at the NE part of the catchment. In the Clement et al., (2017) study also high false flooded area was detected from the area in which extensive agricultural was dominated. Hence, the flooded area detected by the method of histogram thresholding was 5.17 times larger than the flooded area detected by the method of change detection in applying the same polarization of S-1 data. Based on the accuracy assessment presented so far the histogram thresholding method and VV polarization has significant limitation for flood inundation mapping in the area characterize with heterogeneous like as of Akaki catchment. Overall the finding of this demonstrated that parameter (polarization) of S-1 data was highly influence the flood inundation map accuracy than the method used for flood detection.

5 CONCLUSION AND RECOMMENDATION

5.1 Conclusion

In this study, 80 S-1 SAR dataset was used for flood hazard map using Google Earth Engine (GEE) by implementing JavaScript. Change detection (Root of Normalized Image Difference) and Histogram thresholding were compared using co-polarization (VV) and cross-polarization (VH) of the S-1 data. Field surveyed data of the flooded and non-flooded area served as reference to evaluate the methods and polarizations as the date of satellite overpass (09 September 2020).

Reference image affects the accuracy value of flood map detected using change detection method. The January 6, 2019, image fulfilled the minimum irregularity index from all candidates reference image over the analysis period (the dry season of January 2017 to 2020). The January, 25 2020 contained low irregularity index than other dry season image of 2020. Use of the January, 06 2019 image as reference generate high accuracy flood map of 09 September 2020 than using the January, 25 2020. This indicates that acquiring the reference and flooded (target) image from the same year is not a mandatory during flood mapping by change detection method using S-1 SAR image. The analysis in this study revealed the best performing (single) reference image can be used for various flood season of the Akaki catchment.

Histogram thresholding method is dependent on the volume of signal backscatter intensity generated from the flooded and non-flooded surface. It was found to manually fix the threshold to distinguish the flooded and the land surface of the Akaki catchment. Particularly, this soil moisture content of the farm land lands situated at the North-East part of the catchment generated false positive flooded pixels. As the result the flood map generated by the histogram thresholding method has lower accuracy than that of the change detection method.

In this study the VH polarization resulted in better accuracy of flood inundation mapping than the VV polarization. Moreover, the RNID change detection method performed better than the histogram thresholding method in detecting urban and peri-urban flood. Higher flood detection accuracy was obtained when the flood depths are greater than 20cm.

The S-1 satellite overpass the study area once per twelve days interval. Hence, it misses some flood event that occur between consecutive intervals. However, this study demonstrates that S-1 can still provide useful flood information when long time series of images are analyzed.

The remote sensing analysis indicated that the flood started in May and receded in November, but frequent and widespread flood was detected from June to September. It also indicated large inter-annual variation of flood extent in the Akaki catchment. The irrigated land and urban LULC were highly affected by the flood.

Overall the finding of this demonstrated the importance of selecting suitable flood inundation mapping method based on accuracy assessment using field data. It also showed that the different polarization images should be compared and the best performing polarization image should be selected for flood detection instead of arbitrarily selecting the image of S-1 SAR dataset. The RNID change method and VH polarization can be used for continues monitoring of flood hazard in the Akakai catchment.

5.2 Recommendation

The main recommendations based on the methods and results obtained in the study are presented as follows: -.

- The accuracy of the flood inundation map is successfully validated against the field data in this study. Hence, future studies can evaluate the application of these images for participatory flood risk management in this study area.
- Sufficient GCPs are required to validate and increase the accuracy of flood inundation maps generated from remote sensing dataset. However, collecting spatially distributed GCPs from flooded and non-flooded surface area entire Akaki catchment at the date of satellite overpass require community engagement. Therefore, a citizen scientists approach is recommended to collect spatially distributed GCPs at date of satellite overpass.
- It is life threating to collect GCPs from the flooded area that has high depth and velocity. These area can be monitored by installing the staff gauge.
- The twelve-day revisit time of S-1 is one of the major limitations for flood mapping. Some flood event can be missed during the non-revisit date of the S-1 satellite. Therefore, integrating (fusing) different satellites dataset with S-1 is recommended to reduce long revisit time of the satellite.
- In this study flood hazard map was generated. In the future this flood hazard map integrated with the flood exposure of the community and properties for flood risk assessment.

REFERENCE

András Gulácsi and Ferenc Kovács.(2020). Sentinel-1-Imagery-Based High-Resolution Water Cover Detection on Wetlands , Aided by Google Earth Engine. 1–20. Remote Sens. 2020, 12(10), 1614; https://doi.org/10.3390/rs12101614.

Andreoli, R., & Yesou, H. (2007). Change detection analysis dedicated to flood monitoring using envisat wide swath mode data. European Space Agency, (Special Publication) ESA SP, SP-636, 1–6.

Anusha, N., & Bharathi, B. (2019). Flood detection and flood mapping using multi-temporal synthetic aperture radar and optical data. The Egyptian Journal of Remote Sensing and Space Sciences, xxxx, 1–13. https://doi.org/10.1016/j.ejrs.2019.01.001

Argaz, A., Ouahman, B., Darkaoui, A., Bikhtar, H., Ayouch, E., & Lazaar, R. (2019). Flood Hazard Mapping Using remote sensing and GIS Tools : A case study of Souss Watershed. 2508(2001), 170–181.

Arseni, M., Rosu, A., Calmuc, M., Calmuc, V. A., Iticescu, C., & Georgescu, L. P. (2020). Development of Flood Risk and Hazard Maps for the Lower Course of the Siret River , Romania https://doi.org/10.3390/su12166588.

Banko, G. (1998). A review of assessing the accuracy of and of methods including remote sensing data in forest inventory. Internation Institute for Applied Systems Analysis, Interim Report IT-98-081, November, Laxenburg,_ Austria. http://pure.iiasa.ac.at/5570.

Bayik, C., Abdikan, S., Ozbulak, G., Alasag, T., Aydemir, S., Sanli, F. B., Faculty, E., & Faculty, C. E. (2018). Exploiting multi-temporal sentinel-1 sar data for flood extend mapping. XLII(March), 18–21 https://doi.org/10.5194/isprs-archives-XLII-3-W4-109-2018.

Bhatthttps, C. M., Rao, G. S., Farooq, M., Manjusree, P., Shukla, A., Sharma, S. V. S. P., Kulkarni, S. S., Begum, A., Diwakar, P. G., & Dadhwal, V. K. (2017). Satellite-based assessment of the catastrophic Jhelum floods of September 2014 , Jammu & Kashmir , India. Geomatics, Natural Hazards and Risk, 8(2), 309–327. https://doi.org/10.1080/19475705.2016.1218943

Bioresita, F., Puissant, A., Stumpf, A., & Malet, J. P. (2018). A method for automatic and rapid mapping of water surfaces from Sentinel-1 imagery. Remote Sensing, 10(2). https://doi.org/10.3390/rs10020217

Birhanu, D., Kim, H., Jang, C., & Park, S. (2016). Flood Risk and Vulnerability of Addis Ababa City Due to Climate Change and Urbanization. Procedia Engineering, 154, 696–702. https://doi.org/10.1016/j.proeng.2016.07.571

Broich, M., Tulbure, M. G., Broich, M., Stehman, S. V, & Kommareddy, A. (2016). Surface Water Extent Dynamics from Three Decades of Seasonally Continuous Landsat Time Series at Subcontinental Scale in a Semi-Arid Region. Remote Sensing of Environment, 178(June), 142–157. https://doi.org/10.1016/j.rse.2016.02.034

Bucha, N. M., & Selvaraj, R. (2019). Flood inundation mapping in gelana in ethiopia . GSJ 7 May, 148–158.

Caprioli, M., & Tarantino, E. (2001). Accuracy assessment of per-field classification integrating very fine spatial resolution satellite imagery with topographic data Accuracy Assessment of Per-Field Classification Integrating Very Fine Spatial. January https://www.researchgate.net/publication/228775980

Chini, M., Pelich, R., Pulvirenti, L., Pierdicca, N., Hostache, R., & Matgen, P. (2019). Sentinel-1 InSAR Coherence to Detect Floodwater in Urban Areas : Houston and Hurricane Harvey as A Test Case. 1–20. https://doi.org/10.3390/rs11020107

Chini, M., Pulvirenti, L., Pelich, R., Pierdicca, N., Hostache, R., & Matgen, P. (2018). Monitoring urban floods using sar interferometric observations Luxembourg Institute of Science and Technology (LIST), Luxembourg ; CIMA Research Foundation , Italy ; 8785–8788.

Cian, F., Marconcini, M., Ceccato, P., & Giupponi, C. (2018). Flood depth estimation by means of high-resolution SAR images and lidar data. Nat. Hazards Earth Syst. Sci., 18, 3063–3084, 2018. https://doi.org/10.5194/nhess-18-3063-2018

Clement, M., Kilsby, C., & Moore, P. (2017). Multi-Temporal SAR Flood Mapping using Change Detection Multi-temporal synthetic aperture radar fl ood mapping using change detection. April. https://doi.org/10.1111/jfr3.12303

Conde, F. C., & De Mata Muñoz, M. (2019). Flood monitoring based on the study of Sentinel-1 SAR images: The Ebro River case study. Water (Switzerland), 11(12), 1–25. https://doi.org/10.3390/w11122454

Dacosta, O. J., Matthew, E., & Jnr, O. (2019). Long Term Monitoring of Ghana ' s Forest Reserves

Using Google Earth Engine. August. https://doi.org/10.20944/preprints201909.0016.v1

Dadhich, G., Miyazaki, H., & Babel, M. (2019). Applications of sentinel-1 synthetic aperture radar imagery for floods damage assessment: A case study of nakhon si thammarat, Thailand. International Archives of the Photogrammetry, Remote Sensing and Spatial Information Sciences - ISPRS Archives, 42(2/W13), 1927–1931. https://doi.org/10.5194/isprs-archives-XLII-2-W13-1927-2019

Devries, B., Huang, C., Armston, J., Huang, W., Jones, J. W., & Lang, M. W. (2020). Remote Sensing of Environment Rapid and robust monitoring of flood events using Sentinel-1 and Landsat data on the Google Earth Engine. Remote Sensing of Environment, 240(October 2018), 111664. https://doi.org/10.1016/j.rse.2020.111664

Duan, M., & Liu, Z. (2014). Use of remote sensing and gis for flood hazard mapping in use of remote sensing and gis for flood hazard. May 2012.

Eng, J. C. E., Ys, G., & Sl, G. (2015). Flood Hazard Assessment and Mapping of Flood Inundation Area of the Awash River Basin in Ethiopia using GIS and HEC-GeoRAS / HEC-RAS Model. 5(4). https://doi.org/10.4172/2165-784X.1000179

Fekadu, A., Teka, D., & Teka, K. (2017). Integration of Remote Sensing and Hydraulic Models to Identify Flood Prone Areas in Woybo River Catchment , South Western Ethiopia Geography & Natural Disasters. 7(1), 1–13. https://doi.org/10.4172/2167-0587.1000190

Feyissa, G., Zeleke, G., Gebremariam, E., & Bewket, W. (2018). GIS based quantification and mapping of climate change vulnerability hotspots in Addis Ababa. Geoenvironmental Disasters, 5(1). https://doi.org/10.1186/s40677-018-0106-4

Ganji, K., Gharachelou, S., & Ahmadi, A. (2019). Urban'S River Flood Analysing Using Sentinel-1 Data Case Study: (Gorganrood, Aq'Qala). ISPRS - International Archives of the Photogrammetry, Remote Sensing and Spatial Information Sciences, XLII-4/W18(October), 415–419. https://doi.org/10.5194/isprs-archives-xlii-4-w18-415-2019

Gashaw, W., & Legesse, D. (2011). Flood Hazard and Risk Assessment Using GIS and Remote Sensing in Fogera Woreda , Northwest Ethiopia. https://doi.org/10.1007/978-94-007-0689-7

Gebre SL, G. Y. (2015). Flood Hazard Assessment and Mapping of Flood Inundation Area of the Awash River Basin in Ethiopia using GIS and HEC-GeoRAS/HEC-RAS Model. Journal of

Civil & Environmental Engineering, 05(04). https://doi.org/10.4172/2165-784x.1000179

Gouveia, N. D. A., Alves, F. C., & Oliveira, L. De. (2019). Pre-processing of Sentinel-1 C-band SAR images based on incidence angle correction for dark target detection Pre-processing of Sentinel-1 C-band SAR images based on. Remote Sensing Letters, 10(10), 939–948. https://doi.org/10.1080/2150704X.2019.1634300

Gumma, M. K., Amede, T., Getnet, M., Pinjarla, B., Panjala, P., Legesse, G., Tilahun, G., Van Den Akker, E., Berdel, W., Keller, C., Siambi, M., & Whitbread, A. M. (2020). Assessing potential locations for flood-based farming using satellite imagery: A case study of Afar region, Ethiopia. Renewable Agriculture and Food Systems. https://doi.org/10.1017/S1742170519000516

Haoming Xia , Jinyu Zhao, Yaochen Qin, Jia Yang, Yaoping Cui.(2019),Changes in Water Surface Area during 1989 – 2017 in the Huai River Basin using Landsat Data and Google Earth Engine. 1–18. Remote Sens., 11(15), 1824; https://doi.org/10.3390/rs11151824

Hostache, R., Matgen, P., & Wagner, W. (2012a). Change detection approaches for flood extent mapping: How to select the most adequate reference image from online archives? International Journal of Applied Earth Observation and Geoinformation, 19(1), 205–213. https://doi.org/10.1016/j.jag.2012.05.003

Hostache, R., Matgen, P., & Wagner, W. (2012b). International Journal of Applied Earth Observation and Geoinformation Change detection approaches for flood extent mapping : How to select the most adequate reference image from online archives ? International Journal of Applied Earth Observations and Geoinformation, 19, 205–213. https://doi.org/10.1016/j.jag.2012.05.003

Hussain, M., Chen, D., Cheng, A., Wei, H., & Stanley, D. (2013). Change detection from remotely sensed images: From pixel-based to object-based approaches. ISPRS Journal of Photogrammetry and Remote Sensing, 80(January 2018), 91–106. https://doi.org/10.1016/j.isprsjprs.2013.03.006

Jalayer, F., Risi, R. De, Paola, F. De, Giugni, M., Gasparini, P., Topa, M. E., Yonas, N., Yeshitela, K., Cavan, G., Lindley, S., Printz, A., & Renner, F. (2014). Probabilistic GIS-based method for delineation of urban flooding risk hotspots. Claudio 21 , 80125 Naples , Italy. March.

https://doi.org/10.1007/s11069-014-1119-2

Kari, B., Reistad, S., Petersen-øverleir, A., & Bogetveit, L. J. (2014). Setting up rating curves using HEC-RAS. August.

Kianfar, N. (2019). The applicability of dual polarized sentinel-1 sar data for detection of flooded areas in pol-e dokhtar , lorestan , iran. Xlii(october), 12–14.

Klonner, C. (2020). Participatory Mapping and Visualization of Local Knowledge : An Example from Eberbach , Germany. https://doi.org/10.1007/s13753-020-00312-8

Li, Y., Martinis, S., Plank, S., & Ludwig, R. (2018). Int J Appl Earth Obs Geoinformation An automatic change detection approach for rapid fl ood mapping in Sentinel-1 SAR data. 73(March), 123–135. https://doi.org/10.1016/j.jag.2018.05.023

Liang, J., & Liu, D. (2020). ISPRS Journal of Photogrammetry and Remote Sensing A local thresholding approach to flood water delineation using Sentinel-1 SAR imagery. ISPRS Journal of Photogrammetry and Remote Sensing, 159(February 2019), 53–62. https://doi.org/10.1016/j.isprsjprs.2019.10.017

Lin, Y. N., Yun, S. H., Bhardwaj, A., & Hill, E. M. (2019). Urban flood detection with Sentinel-1Multi-Temporal Synthetic Aperture Radar (SAR) observations in a Bayesian framework: A case study for Hurricane Matthew. Remote Sensing, 11(15), 1–22. https://doi.org/10.3390/rs11151778

Liu, J., Xu, Z., Chen, F., Chen, F., & Zhang, L. (2019). Flood Hazard Mapping and Assessment on the Angkor World Heritage Site , Cambodia. 1–19. https://doi.org/10.3390/rs11010098

Long, S. A., Fatoyinbo, T. E., & Frederick, P. (2014). Simplified change detection method for flood extent mapping using SAR. Environ. Res. Lett. 9 (2014) 035002 (9pp) doi:10.1088/1748-9326/9/3/035002

Lu, D., & Moran, E. (2004). Change Detection Techniques. May 2014. https://doi.org/10.1080/0143116031000139863

Mahdianpari, M., Salehi, B., Mohammadimanesh, F., Homayouni, S., & Gill, E. (2019). The first wetland inventory map of newfoundland at a spatial resolution of 10 m using sentinel-1 and sentinel-2 data on the Google Earth Engine cloud computing platform. Remote Sensing,

11(1). https://doi.org/10.3390/rs11010043

Manjusree, P., Prasanna Kumar, L., Bhatt, C. M., Rao, G. S., & Bhanumurthy, V. (2012). Optimization of threshold ranges for rapid flood inundation mapping by evaluating backscatter profiles of high incidence angle SAR images. International Journal of Disaster Risk Science, 3(2), 113–122. https://doi.org/10.1007/s13753-012-0011-5

Martinis, S., & Plank, S. (2018). The Use of Sentinel-1 Time-Series Data to Improve Flood Monitoring in Arid Areas. 1. https://doi.org/10.3390/rs10040583

Martinis, S., & Rieke, C. (2015). Backscatter Analysis Using Multi-Temporal and Multi-Frequency SAR Data in the Context of Flood Mapping at River Saale, Germany. January 2011, 7732–7752. https://doi.org/10.3390/rs70607732

Mohd Hasmadi, I., & Kamaruzam, J. (2008). Satellite data classification accuracy assessment based from reference dataset. International Journal of Computer and Information Science and Engineering, 2(2), 96–102. http://www.waset.org/publications/7672

Muhadi, N. A., Abdullah, A. F., Bejo, S. K., Mahadi, M. R., & Mijic, A. (2020). Image segmentation methods for flood monitoring system. Water (Switzerland), 12(6), 1–10. https://doi.org/10.3390/w12061825

Mutanga, O., & Kumar, L. (2019). Google earth engine applications. Remote Sensing, 11(5), 11–14. https://doi.org/10.3390/rs11050591

Nakmuenwai, P., Yamazaki, F., & Liu, W. (2017). Automated extraction of inundated areas from multi-temporal dual-polarization radarsat-2 images of the 2011 central Thailand flood. Remote Sensing, 9(1), 1–19. https://doi.org/10.3390/rs9010078

Nkomeje, F. (2017). Comparative Performance of Multi-Source Reference Data to Assess the Accuracy of Classified Remotely Sensed Imagery : Example of Landsat 8 OLI Across Kigali City-Rwanda 2015 Felicien Nkomeje To cite this version : HAL Id : hal-01455461 Comparative Perform.

O'Hara, R., Green, S., & McCarthy, T. (2019). The agricultural impact of the 2015-2016 floods in Ireland as mapped through Sentinel 1 satellite imagery. Irish Journal of Agricultural and Food Research, 58(1), 44–65. https://doi.org/10.2478/ijafr-2019-0006

Pekel, J. F., Cottam, A., Gorelick, N., & Belward, A. S. (2016). High-resolution mapping of global surface water and its long-term changes. Nature, 540(7633), 418–422. https://doi.org/10.1038/nature20584

Reksten, J. H., & Solberg, R. (2019). Flood detection in Norway based on sentinel-1 sar imagery. International Archives of the Photogrammetry, Remote Sensing and Spatial Information Sciences - ISPRS Archives, 42(3/W8), 349–355. https://doi.org/10.5194/isprs-archives-XLII-3-W8-349-2019

Risi, R. De, Jalayer, F., Paola, F. De, & Carozza, S. (2020). From flood risk mapping toward reducing vulnerability : the case of Addis Ababa. Natural Hazards, 100(1), 387–415. https://doi.org/10.1007/s11069-019-03817-8

Rose, E. D., Johnson, A. O., & Abubakar, I. (2014). Flood hazard assessment of River Dep floodplains in North-Central Nigeria. International Journal of Water Resources and Environmental Engineering, 6(2), 67–72. https://doi.org/10.5897/ijwree2013.0457

Rwanga, S. S., & Ndambuki, J. M. (2017). Accuracy Assessment of Land Use/Land Cover Classification Using Remote Sensing and GIS. International Journal of Geosciences, 08(04), 611–622. https://doi.org/10.4236/ijg.2017.84033

Saad, A., Milewski, A., Benaabidate, L., El, Z., El, A., & Bouchaou, L. (2019). Flood Frequency Analysis and Urban Flood Modelling of Sidi Ifni Basin , Southern Morocco. 8(5), 206–212. https://doi.org/10.5923/j.ajgis.20190805.02

Schlaffer, S., Matgen, P., Hollaus, M., & Wagner, W. (2015). Flood detection from multi-temporal SAR data using harmonic analysis and change detection. International Journal of Applied Earth Observation and Geoinformation, 38, 15–24. https://doi.org/10.1016/j.jag.2014.12.001

Shen, X., Wang, D., Mao, K., Anagnostou, E., & Hong, Y. (2019). Inundation extent mapping by synthetic aperture radar: A review. Remote Sensing, 11(7), 1–17. https://doi.org/10.3390/RS11070879

Singh, B. K. (2014). Flood Hazard Mapping with Participatory GIS: The Case of Gorakhpur. Environment and Urbanization Asia, 5(1), 161–173. https://doi.org/10.1177/0975425314521546

Skakun, S., Kussul, N., Shelestov, A., & Kussul, O. (2014). Flood Hazard and Flood Risk

Assessment Using a Time Series of Satellite Images : A Case Study in Namibia. 34(8). https://doi.org/10.1111/risa.12156

Stephanie Long , Temilola E Fatoyinbo and Frederick Policelli.(2014). Flood extent mapping for Namibia using change detection and thresholding with SAR. Environ. Res. https://doi.org/10.1088/1748-9326/9/3/035002

Sullivan-wiley, K. A., Short, A. G., & Casellas, J. P. (2019). Mapping vulnerability : Opportunities and limitations of participatory community mapping. Applied Geography, 105(February), 47–57. https://doi.org/10.1016/j.apgeog.2019.02.008

Surampudi, S., & Yarrakula, K. (2019). Mapping and assessing spatial extent of floods from multitemporal synthetic aperture radar images: a case study on Brahmaputra River in Assam State, India. Environmental Science and Pollution Research. https://doi.org/10.1007/s11356-019-06849-6

Tavus, B., Kocaman, S., Gokceoglu, C., & Nefeslioglu, H. A. (2018). Considerations On The Use Of Sentinel-1 Data In Flood Mapping In Urban Areas : Ankara (Turkey). FLOODS. XLII(November), 20–23.

Thakur, P. K., & Sumangala, A. (2000). Flood inundation mapping and 1-d hydrodynamic modeling using remote sensing and gis technique. October.

Thapa, S., Shrestha, A., Lamichhane, S., & Adhikari, R. (2020). Journal of Hydrology : Regional Studies Catchment-scale fl ood hazard mapping and fl ood vulnerability analysis of residential buildings : The case of Khando River in eastern Nepal. Journal of Hydrology: Regional Studies, 30(June), 100704. https://doi.org/10.1016/j.ejrh.2020.100704

Thi, H., Nguyen, T., Doan, T. M., Tomppo, E., & Mcroberts, R. E. (2020). Land Use / Land Cover Mapping Using Multitemporal Sentinel-2 Imagery and Four Classification Methods—A Case Study from Dak Nong, Vietnam. 1–27. https://doi.org/10.3390/rs12091367

Tingsanchali, T., Karim, F., Tingsanchali, T., & Karim, F. (2010). Flood-hazard assessment and risk-based zoning of a tropical flood plain : case study of the Yom River , Thailand Flood-hazard assessment and risk-based zoning of a tropical flood plain : case study of the Yom River , Thailand. 6667. https://doi.org/10.1080/02626660903545987

Tsyganskaya, V., Martinis, S., Marzahn, P., & Ludwig, R. (2018). Detection of temporary flooded

vegetation using Sentinel-1 time series data. Remote Sensing, 10(8). https://doi.org/10.3390/rs10081286

Venkatappa, M., Sasaki, N., & Anantsuksomsri, S. (2020). Applications of the Google Earth Engine and Phenology-Based Threshold Classification Method for Mapping Forest Cover and Carbon Stock Changes in Siem Reap Province , Cambodia. October. Remote Sens. 2020, 12(18), 3110; https://doi.org/10.3390/rs12183110.

Verde, N., Kokkoris, I. P., Georgiadis, C., & Kaimaris, D. (2020). National Scale Land Cover Classification for Ecosystem Services Mapping and Assessment , Using Multitemporal Copernicus EO Data and Google Earth Engine. *Remote Sens.*, *12*(20), 3303; Remote Sens. 2020, 12(20), 3303; https://doi.org/10.3390/rs12203303

Viana, C. M., Girão, I., & Rocha, J. (2019). Long-term satellite image time-series for land use/land cover change detection using refined open source data in a rural region. Remote Sensing, 11(9). https://doi.org/10.3390/rs11091104

Wang, Chao., Jia, Mingming., Chen, Nengcheng., & Wang, Wei. (2018). Long-Term Surface Water Dynamics Analysis Based on Landsat Imagery and the Google Earth Engine Platform : A Case Study in the Middle Yangtze River Basin. https://doi.org/10.3390/rs10101635

Wondim, Y. K. (2016). Flood Hazard and Risk Assessment Using GIS and Remote Sensing in Lower Awash Sub-basin , Ethiopia. 6(9), 69–86.

Woube, M. (1999). Flooding and sustainable land – water management in the lower Baro – Akobo river basin , Ethiopia. 19, 235–251.

Yommy, A. S., Liu, R., & Wu, A. S. (2015). SAR image despeckling using refined lee filter. Proceedings - 2015 7th International Conference on Intelligent Human-Machine Systems and Cybernetics, IHMSC 2015, 2, 260–265. https://doi.org/10.1109/IHMSC.2015.236

Yu Li, Sandro Martinis, Marc Wieland, Stefan Schlaffer and Ryo Natsuaki. (2019). Urban Flood Mapping Using SAR Intensity and Interferometric Coherence via Bayesian Network Fusion. remote sensing. https://doi.org/10.3390/rs11192231.

Yuan, C., Wang, F., Wang, S., & Zhou, Y. (2019). Accuracy evaluation of flood monitoring based on multiscale remote sensing for different landscapes. Geomatics, Natural Hazards and Risk, 10(1), 1389–1411. https://doi.org/10.1080/19475705.2019.1580224

Zeng, Z., Gan, Y., Kettner, A. J., Yang, Q., Zeng, C., & Brakenridge, G. R. (2020). Towards high resolution fl ood monitoring : An integrated methodology using passive microwave brightness temperatures and Sentinel synthetic aperture radar imagery. Journal of Hydrology, 582(May 2019), 124377. https://doi.org/10.1016/j.jhydrol.2019.124377

Zhang, M., Chen, F., Liang, D., Tian, B., & Yang, A. (2020). Use of Sentinel-1 GRD SAR Images to Delineate Flood Extent in Pakistan. Sustainability, 12(14), 5784. https://doi.org/10.3390/su12145784

Zhang, W., Hu, B., & Brown, G. S. (2020). Automatic Surface Water Mapping Using Polarimetric SAR Data for Long-Term Change Detection. water, 1–14 https://doi.org/10.3390/w12030872.

Zhuang, H., Fan, H., Deng, K., & Yu, Y. (2018). An improved neighborhood-based ratio approach for change detection in SAR images. European Journal of Remote Sensing, 51(1), 723–738. https://doi.org/10.1080/22797254.2018.1482523

Annex

Annex A: Field plan (guide map) used to collect GCPs from the flooded and non-flooded area at the date of satellite overpass.

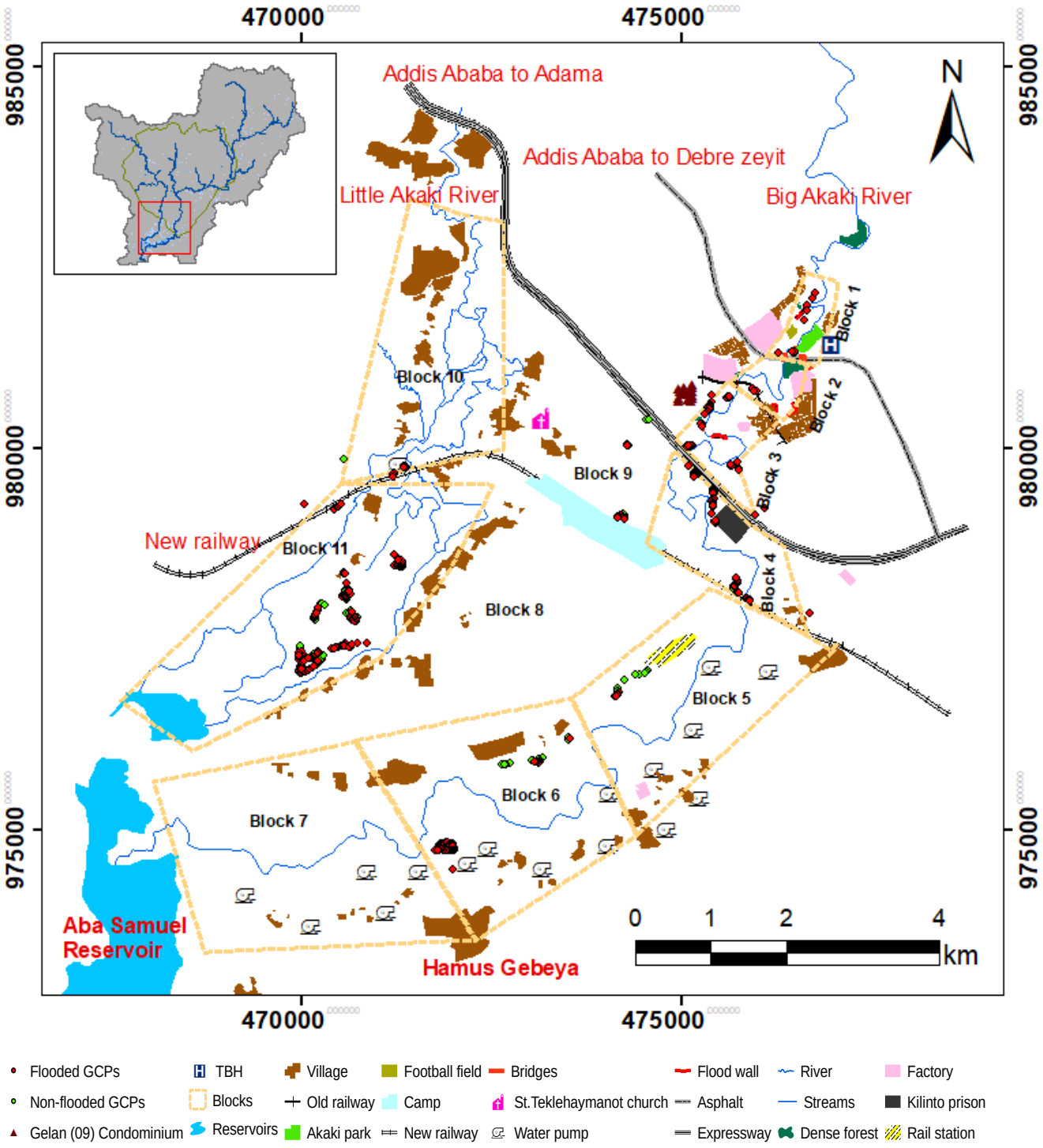

Annex B

Pictures taken during field inventory at the downstream of expressway (Addis Ababa to Adama) just Kilinto prison.

Annex C : - The error matrix for the flood inundation map generated by using histogram thresholding method and, VV polarization.

	Reference data(GCPs)				
Classified	Flooded	Non-flooded	∑	User's accuracy	Commission error
Flooded	133	46	179	74.30%	25.7%
Non-Flooded	3	51	54	94.44%	5.56%
∑	136	97			
Producer's accuracy	97.79%	52.58%			
Omission error	2.21%	47.42%			

Annex E:- Error matrix of the flood map generated using change detection method and VV polarization

	Reference data(GCPs)				
Classified	Flooded	Non-flooded	∑	User's accuracy	Commission error
Flooded	152	27	179	84.9%	15.1%
Non-Flooded	4	50	54	92.6%	7.4%
∑	156	77			
Producer's accuracy	97.4%	64.9%			
Omission error	2.6%	35.1%			

The overall accuracy = 86.7% and kappa coefficient = 67.5%.

Annex D

September 09, 2020 flood inundation maps generated using two different reference images. These reference images are collected from January 25, 2020 (has minimum irregularity index from collected January of 2020 candidate images) and the January 06, 2019 (minimum irregularity index from the candidate of January 2017 to 2020). The flooded pixel detected when applying both reference image were labelled as "Both". The flooded pixel detected when applying the January 06, 2019 reference image labelled as "Ref 06012019" and for the January 25, 2020 reference image labelled as 'Ref25012020.

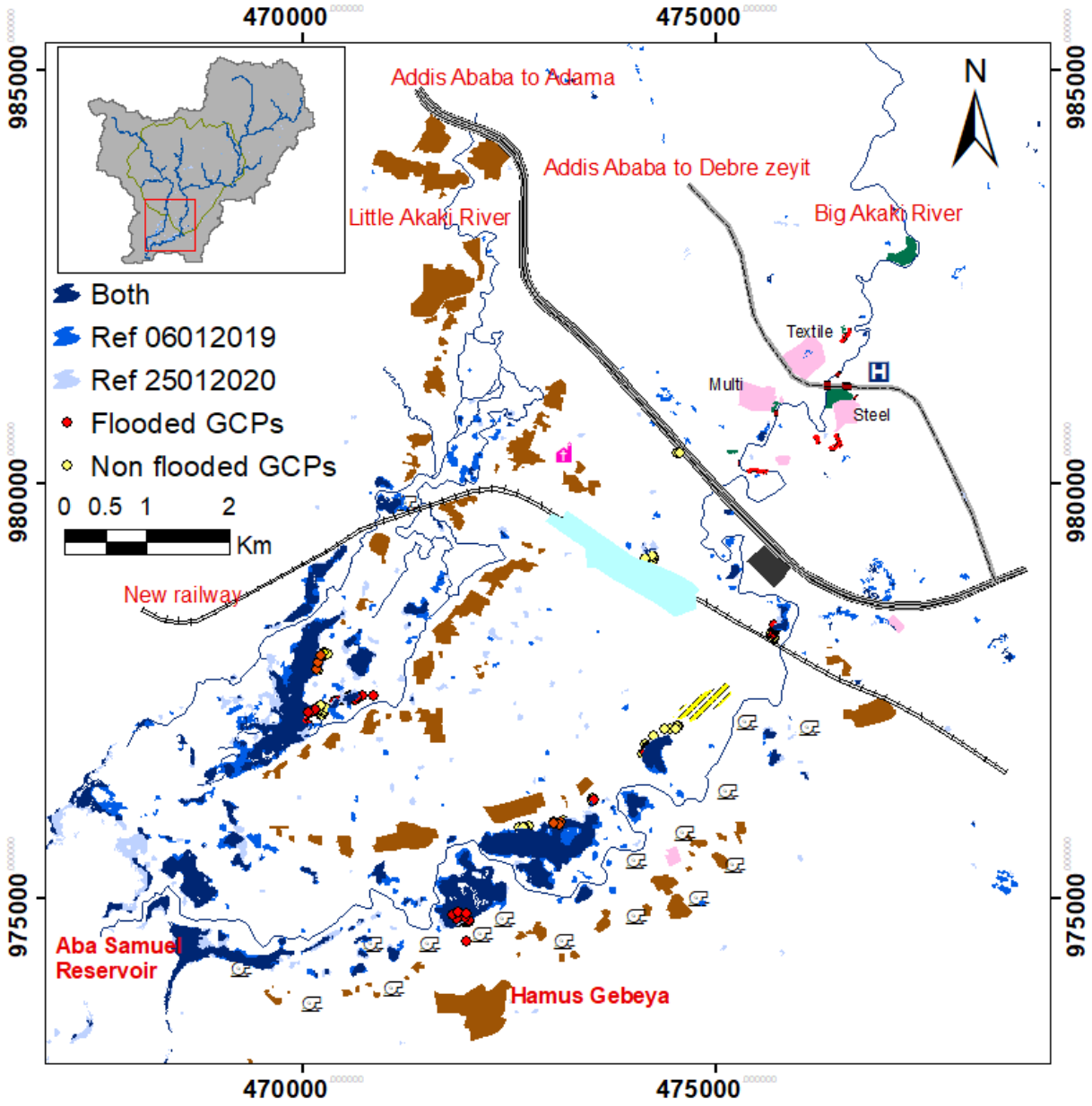

Annex F

Monthly flood frequency maps detected in April to November from 2017 to 2020 left to right sequence.

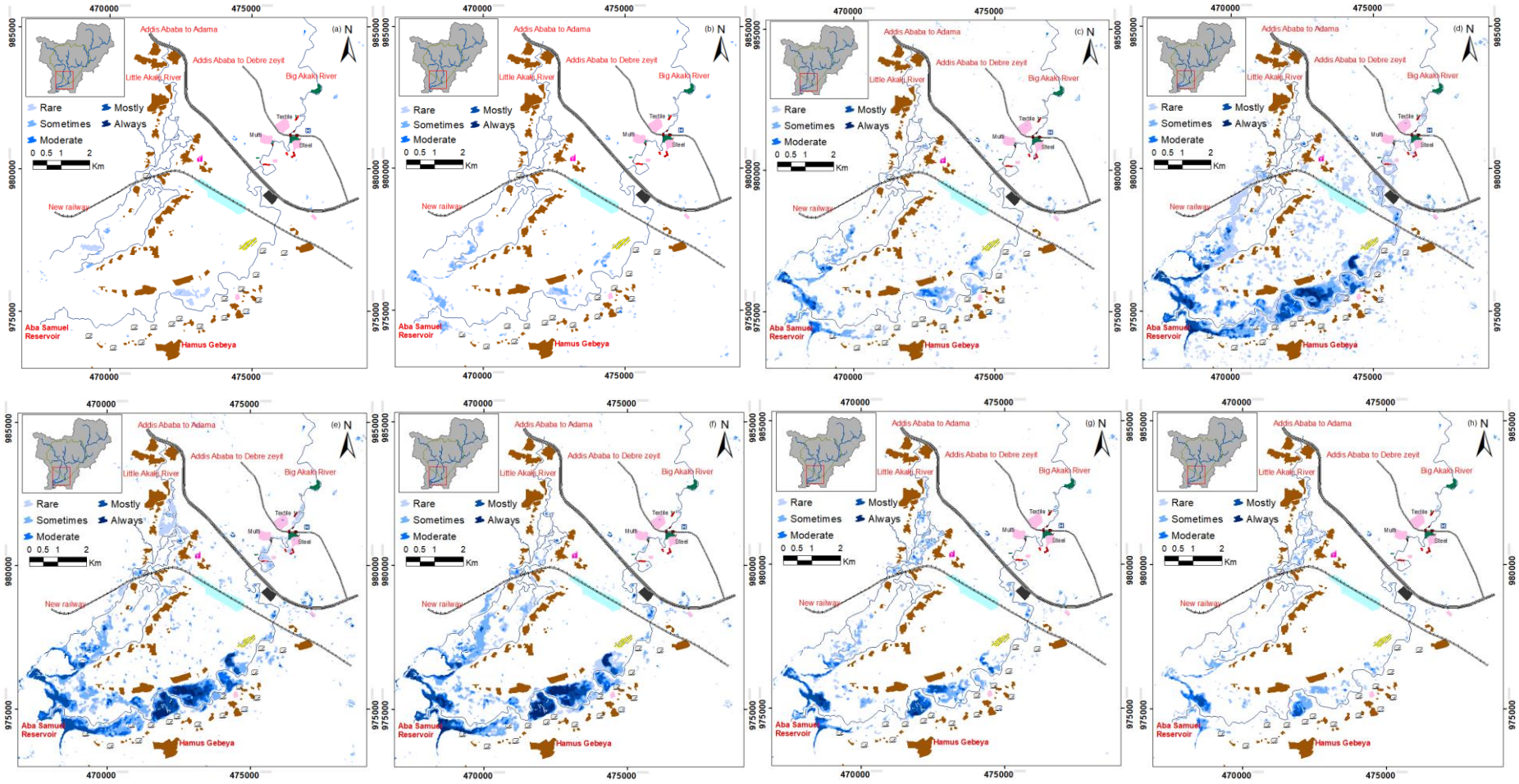

Annex G Annual flood frequency occurrence map detected in 217, 2018, 2019 and 2020 sequence.

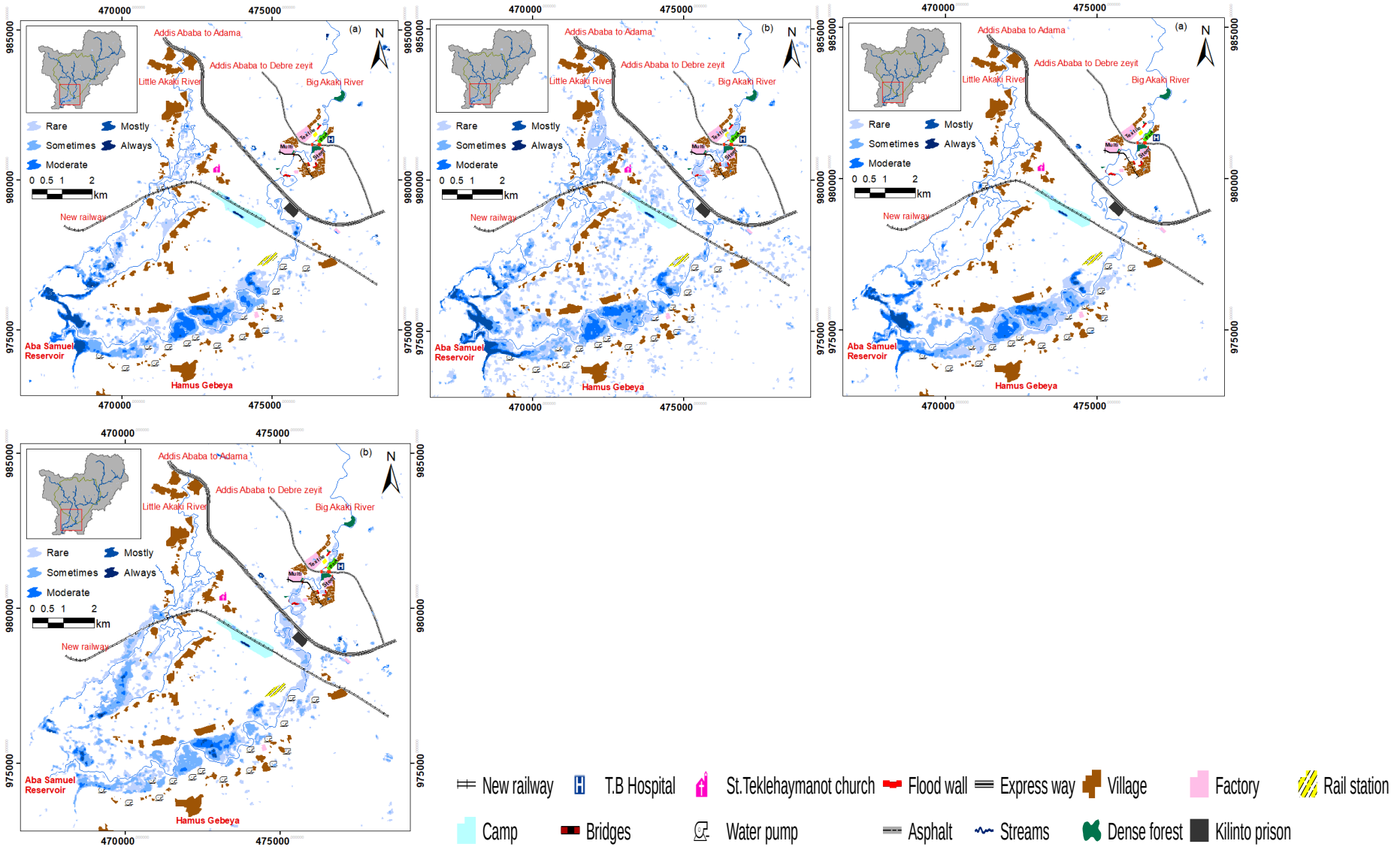

Annex H

Major roads in Addis Ababa affected by flood in the past four years (2017 to 2020) are listed on their sub-city, Wereda, Village name, Roads name and Exact locations.

Labelled	Sub-city	Woreda	Village Name	Road names and location	Exact Location
	Akaki Kality	6	Saris	Saris to Kality	In front of car train (Maseltegna)
M		6		Saris to Abo	Saris to Abo Mazoriya
K		6		Saris Abo to Bole (on ring road)	Abo round in front of Abo church
		6		Ring road	Saris worku sefer on ring road in front of the food complex factory
		5	Kality	Sarsis to Kality	In front of Wiha limat and Alfa university college
		7		Sarsis to Kality	In front of St.Gebriel church
		7		Sarsis to Kality	In front of Crown Hotel
I	**Nifas Silk Lafto**	2	Jemo	Michael taxi mazoriya to Jemo -1	Infront of Anbese Geraj
		2			Infront of sisters Cafe
		2			Jemo-1 Bajaj tera
		2	Lebu	Lebu (mebrat Hail) to Germen round	Near to St. Arsema Church
J		1		Mestawet Factory to Jemo 3 round	Infront of Mestawet Factory and Jemo 3 round
		1		Jemo 1 Condominium to Medhani Alem church	Inside Condominium's on the main Asphalt
		1			Infront of Medhani Alem church
		1		Lebu (Mebrat hail) to Jemo 1	infront of Shewa and Gara Supermarket
		1	Furi	Furi to Nock	Infront of CBE Gara Bolo branch
K		1		Expressway Infront of Sefera Garment	Sefera round
		8	Saris	Saris to Gotera	Infront of Kadisco paint
	Kolfe Keranio	1	Koshe	Jemo to Ayer tena (on ring road)	Infront of solid waste power project
H	**Lideta**	1	Lideta	Lideta	Inside old airport

		2		Tor hayloch to Mexico	Infront of Tor hailoch Hospital
		9	Mexico	Mexico round to Shebele Hotel	Infront of Total gas oil station
		9	Posta Bet	Piassa to Beherawi tiater	Infront of post office
		10		From sarbet to Lideta road	Infront of St.Mickael Church
	Kirkos	7		At the Back of main stadium	Near National Tourist Organization
		7	Legahar	Leghar to Beherawi tiater	At the Back of Ethiopian Medin Insurance
		10		Road Legehar to Kera	At the back of legehar old rail station
G		7		Filwoha to Beherawi tiater	Infront of Ambasader tiater
		1	Meskel Adebaby	Meskel Adebabay to Bole Olompia	Back to Semaetat Musium
		9		Meskel Adebabay	Infront of Meskel Adebabay
		3			Infront of Meskel Flower Hotel
		3		Gotera to Stadion	Infront of Omedla Hotel
	Arada	2	Piassa	Abune Petiros Memorial to Merkato	Infront of Piassa Atikilt tera
	Gulele	2	Sidist Kilo	Sidist kilo	Infront of lion park
		2		Shiromeda	Infront of American Embacy
A	**Bole**	1	Bole	Bole	Inside Air port
		2			Bole Round to Lucy land Hotel
B		3			Infront of Millineum Hall
		3			Infront of Medhane Alem catederal church
D		3			Inside new Stadioum cumpas
		6		Ring road	Infront of Amiche
	Yeka	5	Megenagna	Megenagna Round	infront of Yeka Kifle ketema
		5		Megenagna to Arat kilo	Infront of Kenya Enbasy
C		9		Megenagna to Gurdshola	Infront of ILRI campus and Kaldi's Coffee cafe
E		9		Megenagna to Hayat	Road to Sumit Condominium